Bio-Design and Manufacturing (2023) 6:217–242
https://doi.org/10.1007/s42242-022-00218-y

RESEARCH ARTICLE

Alginate/gelatin/boron-doped hydroxyapatite-coated Ti implants: in vitro and in vivo evaluation of osseointegration

Ahmet E. Pazarçeviren[1] · Zafer Evis[1] · Tayfun Dikmen[2] · Korhan Altunbaş[2] · Mustafa V. Yaprakçı[3] · Dilek Keskin[1,4] · Ayşen Tezcaner[1,4]

Received: 8 June 2022 / Accepted: 30 September 2022 / Published online: 5 January 2023

Abstract

In this study, boron-doped hydroxyapatite (BHT)-loaded alginate/gelatin-based (A/G) hydrogel coating on Ti was fabricated to support bone integration through triggering osteoinduction, vascularization and immunomodulation. Initially, highly reproducible, cheap and time-effective BHT was produced, which significantly promoted higher osteogenic and angiogenic maturation, while a mild innate immune response was observed. The immense potential of BHT was evidenced by the production of a gap-filling A/G/BHT interphase on Ti implants to mimic the osseous extracellular matrix to achieve functional bridging and exert control over the course of innate immune response. We initially aminosilanized the implant surface using 3-aminopropyl triethoxysilane, and then coated it with 0.25% w/v alginate with 20 mM 1-ethyl-3-(3-dimethylaminopropyl) carbodiimide and N-hydroxysuccinimide to allow the A/G/BHT pre-gel to disperse evenly and covalently attach on the surface. The pre-gel was added with 0.2 M NaCl to homogeneously blend BHT in the structure without inducing ionic crosslinking. Then, the coated implants were freeze-dried and stored. The coated layer demonstrated high cohesive and adhesive strength, and 8-month-long shelf-life at room temperature and normal humidity. The A/G/BHT was able to coat an irregularly shaped Ti implant. Osteoblasts and endothelial cells thrived on the A/G/BHT, and it demonstrated greatly improved osteogenic and angiogenic capacity. Moreover, A/G/BHT maintained macrophage viability and generated an acute increase in immune response that could be resolved rapidly. Finally, A/G/BHT was shown to induce the robust integration of implant in a rabbit femur osteochondral model within 2 months. Therefore, we concluded that A/G/BHT coatings could serve as a multifunctional reservoir, promoting the strong and rapid osseointegration of metallic implants.

✉ Ayşen Tezcaner
tezcaner@metu.edu.tr

[1] Department of Engineering Sciences, Middle East Technical University, Ankara, Turkey

[2] Department of Histology and Embryology, Afyon Kocatepe University, Afyon, Turkey

[3] Department of Surgery, Afyon Kocatepe University, Afyon, Turkey

[4] Center of Excellence in Biomaterials and Tissue Engineering, Ankara, Turkey

Graphic abstract

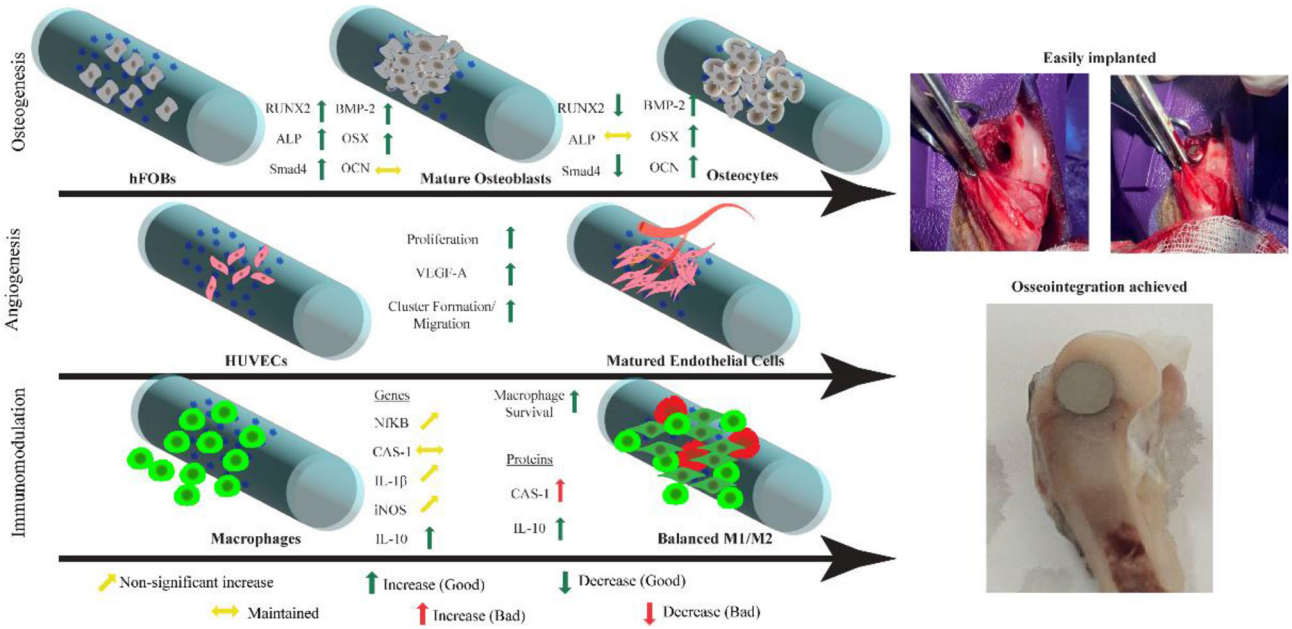

Keywords Boron · Alginate/gelatin · Implant coating · Titanium · Osteochondral model

Introduction

Osseointegration is a multifaceted phenomenon involving diverse pathways acting in concert, bringing about strong and functional bridging between implant and bone. Since the implant-bone fusion depends on several aspects, such as osteogenesis, angiogenesis and immunomodulatory responses, to induce rapid bone deposition, subsequent remodeling and robust integration, it is expected of next-generation implants to show high biological performance while avoiding undesired reactions and supporting regeneration. In this sense, titanium-based implants (Ti) have been modified by various methods to trigger intertwined responses directing osseointegration [1, 2]. Especially focusing on bioactive modifications, Ti has been coated with hydrogels to both provide a reservoir for various biological factors and establish a niche for homing stem cells [3, 4].

Although many Ti implant surface designs have become commercially available, bioceramic coatings comprise a state-of-the-art Ti surface modification for better osseointegration. In this sense, such coatings [5–7] have been studied extensively by various groups; however, Ti implant surfaces require additional modifications to augment biological activity because of the transient and limited support provided by ceramic implantation [8]. Bioceramic particles have low adhesion strength due to the lack of chemical/supramolecular interaction between ceramic particles and the metal surface, which may cause their detachment from the implant surface and drive undesired immunological response [9, 10]. Moreover, direct ceramic-based coatings fail to achieve multifunctionality because of their low applicability in geometrically irregular implants, low control on the final product due to the excessive pressure and heat required to seed bioceramics on the Ti surface, and their inability to load any supplementary biological factors (peptides, miRNA, exosomes, drugs, etc.) [11, 12].

For the above reasons, bioceramics have been successfully utilized as a multifunctional reinforcement in a polymeric matrix to encourage new bone formation at the implant periphery, thus providing additional secondary stability [13–15]. In spite of the tremendous applicability (simple coating method such as dip-coating without use of expensive or complex devices) and pliability of synthetic polymers, they lack natural peptide sequences or patterns that can be recognized by cells. On the other hand, natural polymers tend to mimic natural osseous extracellular matrix (ECM) more effectively in comparison with synthetic counterparts and provide tailorable biosimilar patterns [11]. In addition, synthetic polymers cannot be degraded by natural processes or by macrophages as efficiently as natural polymers [16]. In this context, the use of natural polymer-based matrixes to load bioceramic reinforcements appears as a successful next-generation implant coating

modality to enhance the rate of Ti implant osseointegration.

Alginate (ALG) is a carbohydrate composed of 1,4 α-L-guluronic acid and 1,4 β-mannuric acid monomers [17]. It has –OH and –COOH functional groups that can be modified or used as anchorage points for crosslinking with other polymers [18]. The tailorable chemical and physical structure of alginate makes it one of the most often employed polysaccharides for designing highly responsive ECM-like hydrogels for improved three-dimensional (3D) cell colonization and on-site cargo release [19–21]. In addition, many studies in the literature have demonstrated the tremendous ability of ALG in forming polymer blends with other natural polymers with or without additional modifications [22–25]. Nevertheless, ALG is usually employed along with other biomaterials to reinforce its biological properties. Because of its high negative charge at neutral pH, ALG shows very low immunogenicity [26]; however, stem cells also tend to avoid ALG-coated surfaces [27]. Therefore, ALG requires structural modification to support cellular adhesion.

Gelatin (GEL) is another important natural polymer in the design of ECM mimicking 3D constructs, because it augments the gelation capacity and cohesiveness of polymer-based hydrogels [28]. Additionally, GEL possesses the arginyl-glycyl-aspartic acid (RGD) cell adhesive motif [29] and lacks the immunogenic tertiary collagen conformation [30]. In this sense, ALG-GEL (A/G) hydrogels with low immunogenicity and good biocompatibility could be produced. In the literature, the ALG-GEL combination is indeed one of the most widely used natural polymer blends to fashion 3D constructs showing high capacity for cell encapsulation and proliferation [31], and the release of bioactive molecules [32, 33], antibacterial drugs/ions [34, 35], osteogenic/angiogenic or immunomodulatory factors [36, 37]. However, it was observed that no covalently bonded and structurally stable ALG-GEL-based coatings exist for establishing a functional bone-implant bridge. Such interphases composed of various ALG-GEL coatings were produced and characterized in our previous study [38]. We optimized a robust, strong and long shelf-life (~12 months at 25 °C under normal relative humidity of ~60%) coating on Ti implant with 1% w/v ALG and 3% w/v GEL (A/G coatings). In addition, these coatings were shown to be highly resistant to scratching and did not delaminate after freeze-drying. Therefore, an A/G layer on the Ti implant was deemed to be applicable for loading with a multifunctional bioceramic and suitable for implants placed through press-fitting.

In this study, we loaded A/G with boron-doped hydroxyapatite (BHT) to reinforce its bioactivity by inducing osteogenic/angiogenic/immunomodulatory calcium (Ca) and boron (B) release. Boron, which was doped at 5% molar concentration in hydroxyapatite (HT), was shown to be an osteogenic and angiogenic trace element in previous studies [39–41]. Thus, we utilized BHT as a multifunctional reinforcement that endows immunomodulatory features. With the inclusion of BHT in the A/G matrix, we hypothesized that the pliability and applicability of A/G/BHT as an ECM-like coating could be achieved. In this context, we aimed to homogeneously blend BHT in the A/G pre-gel by reaching the lowest possible amount of interaction between powder particles and the polymer matrix [42]. Since it was shown in the literature that having a low initial ionic bonding followed by strong interaction at the polymer-bioceramic interface provides a highly reproducible method [43], we took these procedures one step forward and aimed to obtain a crack-free, non-delaminating and highly bioactive composite interphase on Ti by inducing covalent bonding between the composite hydrogel matrix and the Ti surface, as well as acquiring intermolecular ionic interactions. Therefore, a relatively simple, straightforward, cost-effective and time-effective methodology was employed to coat both regular and irregularly shaped Ti surfaces.

In the present study, A/G-based composite coating loaded with versatile BHT was produced to support bone integration and act as a highly osteoinductive, angiogenic and immunomodulator interphase. A natural polymer-based hydrogel form having bioceramic reinforcement was selected to mimic natural ECM at the periphery of the defect. The coated gap-filling 3D structure was designed to accommodate stem cells and allow for both bone deposition and vascularization, to boost the rate of osseointegration of the Ti-based implant. Furthermore, this layer was intended to serve as a reproducible and long shelf-life reservoir that can further improve the clinical abilities of metallic implants by allowing the local release of bioactive ions and promote biological responses. The samples were first characterized for their physical, morphological, chemical and biological properties in vitro. Then, they were analyzed in a rabbit osteochondral defect model in vivo to investigate the clinical translation potential of A/G/BHT coating.

Materials and methods

Materials

Calcium nitrate dihydrate ($Ca(NO_3)\cdot 2H_2O$), diammonium phosphate ($(NH_4)_2HPO_4$), boric acid (H_3BO_3), para-nitrophenyl phosphate (pNpp), magnesium chloride ($MgCl_2\cdot 6H_2O$), β-glycerophosphate, 50 μg/mL L-ascorbic acid, 10^{-7} M dexamethasone, Triton X-100, 1-Ethyl-3-(3-dimethylaminopropyl) carbodiimide (EDC), N-hydroxysuccinimide (NHS), sodium chloride (NaCl), sulfuric acid (H_2SO_4), hydrogen peroxide (H_2O_2), sodium hydroxide (NaOH), copper sulfate ($Cu(II)SO_4$), ammonium chloride (NH_4Cl), sodium azide (NaN_3), sodium cacodylate,

paraformaldehyde (PFA) and bovine serum albumin (BSA) were purchased from Sigma-Aldrich, USA. Heat inactivated fetal bovine serum (FBS), 10,000 U/mL penicillin–streptomycin (P/S), DMEM/F12, RPMI 1640, and EndogoXF mix were obtained from Sartorius, Germany. Distilled water was produced by purification through a resin bed, reverse osmosis, and flowing through an ultraviolet (UV) electrodeionization device (Millipore ELIX-5, Sigma, USA).

Characterization of BHT

Hydroxyapatite (HT) and boron hydroxyapatite (BHT) were produced using a wet precipitation/microwave reflux method. $Ca(NO_3)\cdot 2H_2O$ and $(NH_4)_2HPO_4$ were used as Ca and P sources, respectively. H_3BO_3 was utilized as a B source. The Ca source (0.62 M) was dissolved in dH_2O, and the initial pH was set to 9–10 by the addition of NH_4OH. Subsequently, a mixture of P (0.33 M) and B (0.05 M) sources was added dropwise. The mixture was aged under 800 W for 15 min in the reflux system. Then, samples were centrifuged at 8000*g* for 3 min at 4 °C, suspended in pure acetone and homogeneously downsized by a probe sonicator at 25% amplitude for 2 min. After that, the powders were dried at 100 °C and calcined at 1100 °C for 2 h. The Ca and B powders (100 mg/mL) were placed in centrifuge tubes previously added with dH_2O with 0.2% (w/v) sodium azide (NaN_3). The samples were incubated for 2 weeks in this release media with a volume 10 times of the mass of powders. At the end of each week, the amount of element released was determined by induced coupled plasma mass spectroscopy (Perkin Elmer DRC II, ICP-MS (*n*=3)). The physical, mechanical and structural properties of HT and BHT were characterized and compared in our previous study [39].

Osteogenic potential of BHT

HT and BHT were placed in an osteoblast growth medium (DMEM:F12 (94.8%), fetal bovine serum (5%), 100 U penicillin–streptomycin (0.2%)) in 100 mg/mL concentration to prepare the conditioned media. Human fetal osteoblasts (hFOB (hFOB 1.19, ATCC, USA), 5×10^3 per well in a 48-well plate) were incubated in the obtained conditioned media for 1, 4 and 7 days (*n*=12). Cell proliferation was measured at the end of each incubation period with Alamar blue assay using the supplier's protocol (Thermo Fisher, USA).

Cells (2×10^4 per well) were seeded in 24-well plates, and incubated in the conditioned media prepared in an osteogenic induction medium (growth medium added with 10 mM β-glycerophosphate, 50 μg/mL L-ascorbic acid and 10^{-7} M dexamethasone) for 2 weeks (*n*=18). At the end of each week, hFOBs were rinsed with phosphate buffered saline (PBS, 0.01 M, pH 7.4), then lysis buffer (0.1% Triton X-100 in 0.2 M carbonate buffer) was added and three freeze-thaw cycles were initiated at −80 °C. Once the cells were lysed, alkaline phosphatase (ALP) enzyme substrate working solution (10 vol pNpp, 20 vol dH_2O and 1 vol $MgCl_2\cdot 6H_2O$ in dH_2O) was mixed with the lysates in a 1:1 v/v ratio and incubated for 1 h at 37 °C. Afterward, the absorbance of the reaction media was measured at 405 nm. The DNA content of lysates was determined with Picogreen assay using the supplier's protocol (Thermo Fisher Scientific, USA). The ALP activity of hFOBs that had interacted with samples was determined after normalizing the ALP concentration to total DNA content and the time spent (mmol ALP/g_{DNA} min). A similar protocol with ALP activity assay was followed for the osteocalcin (OCN) release study (*n*=8). At the end of each week, the sample media were collected, and enzyme-linked immunosorbent assay was used to quantify the amount of OCN released in accordance with the supplier's protocol (E4762, Biovision, USA). The OCN release data were normalized to the total DNA for each sample. Cells were also seeded in 12-well plates at 4×10^4 per well and interacted with the conditioned media to prompt biomineralization in a setup similar to the ALP activity assay (*n*=2). At the same time, Alizarin red stain (ARS) was dissolved in dH_2O and the pH was set to 4.2 using 10% v/v ammonia in water. At each incubation period, wells (*n*=2) were rinsed with PBS, then ARS (4% w/v) stain was placed in the wells, which were incubated for 30 min at room temperature. Subsequently, the wells were rinsed with dH_2O thrice and images were obtained through a phase contrast microscope.

Total RNA was isolated from hFOBs during osteogenic differentiation analysis in accordance with the supplier's protocol (High Pure mRNA Isolation Kit, Roche, Switzerland) for the quantitative real-time PCR analysis (qPCR) of RUNX2, ALP and OSX. The RNA quality was ensured, quantified, and cDNAs were produced (Applied Biosystems PCR System 9700, USA) using the supplier's protocol (Transcriptor High Fidelity cDNA Kit, Roche, Switzerland). Using the SYBR Green qPCR kit, cDNAs were combined with the primers given in Table S1 (Supplementary Information), and qPCR was conducted (Roche Lightcycler 480, Switzerland). Amplification reactions were performed for 40 cycles, and the cycle number at the detection threshold (C_t) for each sample was determined. Beta-actin was used as the housekeeping gene to determine the cycle threshold (ΔC_t) values for each sample. The relative changes in the gene expression of samples were calculated by the $2^{-\Delta\Delta C_t}$ method.

Angiogenic potential of BHT

HT- and BHT-conditioned media were prepared by incubating the powders at a concentration of 100 mg/mL in EndoGo XF medium and supplement mix (Sartorius, Germany) for

24 h at 37 °C. Human umbilical cord vein endothelial cells (HUVECs) were seeded at a density of 4×10^4 cells/well in 24-well plates, and incubated with the conditioned media for 4 h. Next, media were discarded and Alamar blue assay was conducted (n=6).

For the tube formation and VEGF-A release assay, cold growth factor reduced basement membrane matrix (Matrigel, Corning, USA) was pipetted into 96-well plates (50 μL/well) and incubated in a CO_2 incubator (MCO-5M-PE, Panasonic, Japan) for 30 min for gelation. After seeding HUVECs on the Matrigel, conditioned media were added and incubated for 4 h to achieve the maximum rate of tube formation. At the end of the incubation period, media were collected and stored at −80 °C until further use. PBS was added to the wells, and photographs at five different locations were taken to quantify number of nodes (n=5), total tube area (n=5), and total master segment length (n=5) using the Angiogenesis Analyzer plugin [44] in ImageJ (NIH, USA). Subsequently, cells were lysed using the lysis solution as aforementioned, the media were collected during the tube formation assay, and the lysates were combined in 1:1 v/v. Total VEGF-A production (n=4) was determined using a human VEGF-A ELISA kit (CSB-E11718h, Cusabio, China). The total DNA content of lysates was also measured, and VEGF-A release was normalized to the DNA concentration (mg VEGF-A/g_{DNA}).

Immunomodulation study

THP-1s were incubated in RPMI 1640 medium supplemented with 10% v/v FBS, 0.5% v/v P/S cocktail and 0.1% v/v Normocin (monocyte growth medium). The THP-1s were seeded on cell culture plates at a density of 0.45×10^6 cells/mL and stimulated with 50 ng/mL phorbol 12-myristrate 13-acetate (PMA) for 24 h to adhere on wells and differentiate into macrophages. Thereafter, they were rinsed twice with PBS to completely remove the PMA and then incubated for 24 h in HT- and BHT-conditioned media (100 mg/mL), prepared in RPMI 1640 and 10% v/v FBS. PMA was used as an abbreviation for THP-1s on wells induced with PMA only, to mimic the initial macrophage state (M0). THP-1s denoted as PMA + LPS were initially induced with PMA and primed with 150 ng/mL lipopolysaccharide (LPS from *Escherichia coli* O55:B5, Sigma, USA), and were used for mimicking the inflammatory macrophages (M1). Pro-healing macrophages were denoted as M2.

After incubation, aliquots from each sample (n=4) were collected, centrifuged at 8000g for 10 min and assayed using human caspase-1 (CAS-1, E4588, Biovision, USA), interleukin-10 (IL-10, CSB-E04593h, Cusabio, China), and inducible nitric oxide synthase (iNOS, E4648, Biovision, USA) ELISA kits. Meanwhile, cell viability was determined by Alamar blue assay and total DNA content was determined by Picogreen assay to normalize CAS-1, IL-10 and iNOS release. In addition, THP-1s were visualized by phase contrast microscope to analyze their morphologies after incubation in the conditioned media for 24 h.

Table 1 Samples used in the study

Abbreviation	Coating
Ti-APA	–
A/G	Alginate and gelatin coating
A/G/BHT	Alginate and gelatin coating loaded with BHT

Fabrication and characterization of A/G and A/G/BHT coatings on Ti

Fabrication, rheological, physical and chemical properties

Medical grade titanium alloy (Grade V Ti-6Al-4V ELI, Ti) was modified through acid:peroxide:alkali (APA) to obtain a standard and highly utilized Ti-APA. The Ti was cleaned, sandblasted with garnet and subsequently rinsed with pure ethanol and acetone. Then, Ti was incubated in H_2SO_4:H_2O_2 (3:7 v/v) for 15 min, rinsed twice with dH_2O, and placed in 5 M NaOH for 1 h at 60 °C. Finally, Ti-APA was rinsed with dH_2O and dried in a desiccator. To covalently attach alginate/gelatin (A/G) blend on Ti-APA, 3-Aminopropyl triethoxysilane (APTES) was employed to functionalize the surface with aminosilane, and a modified version of EDC/NHS/$CaCl_2$ chemistry was used [38]. Initially, Ti-APA was coated with a thin layer of 0.25% w/v alginate blended with 20 mM EDC/NHS, to achieve a homogeneous coating. Then, A/G was added with 0.2 M NaCl, 20 mM NHS and homogeneously mixed with BHT (A/G/BHT pre-gel). The different samples used were given in Table S2 (Supplementary Information). After pre-gels were formed (Video S1 in Supplementary Information), the alginate-coated Ti-APA was slowly dipped in A/G or A/G/BHT pre-gel (20 mm/s), kept in for 15 s and taken out (5 mm/s). Thereafter, coated samples were air-dried for 1 h, placed in 20 mM EDC/NHS/$CaCl_2$ crosslinking solution for 1 h, and then rinsed 3 times thoroughly before freeze-drying at −80 °C for 6 h. The samples produced are given in Table 1. All samples were placed in dust-free desiccator until further use (<10% relative humidity, 25 °C). Samples were then coated with gold/palladium and visualized under scanning electron microscopy (SEM, FEI Quanta650, USA).

Rheological analysis was conducted with the pre-gels (20 mL) using smooth concentric cylindrical geometry (DIN standard cup and bob having 14 and 15 mm radii, respectively) in a rotational rheometer (TA Instruments ARES

Rheometer, USA). Changes in the apparent viscosity of samples under increasing shear rate (1–100 s^{-1}) at 40 °C were recorded. The samples were tested for water uptake (n=4) and hydrolytic degradation (n=4) in PBS with 0.02 w/v % NaN_3. The weights of dried samples (w_{D1}) were recorded prior to analysis, and the weights of wet samples (w_{wet}) were measured until the plateau was reached for water uptake analysis. The water uptake is calculated using Eq. (1):

$$\text{Water uptake} = \frac{w_{\text{wet}} - w_{\text{D1}}}{w_{\text{D1}}} \times 100\%. \quad (1)$$

In addition, samples placed in PBS with NaN_3 were incubated for 1–4 weeks under the same conditions as mentioned above. The samples were thoroughly rinsed, freeze-dried for 24 h, their weights were recorded (w_{Di}), and weight loss was calculated in accordance with Eq. (2):

$$\text{Weight loss} = \frac{w_{\text{D1}} - w_{\text{D}i}}{w_{\text{D1}}} \times 100\%. \quad (2)$$

In order to confirm attachment on the surface, samples were manually tested to observe if delamination occurred during degradation or swelling (data not shown). After making sure that none of the samples showed any cracks or delamination, subsequent analyses were conducted.

Methylene blue (MB) was used as a dye to determine the loading/release feature of coatings as a reservoir. A MB solution was prepared in 0.5% (w/v) PBS/NaN_3. The samples were placed in wells, were added with 1 mL MB solution, and were incubated for 15 min, 1, 3, 6 and 24 h. MB loading was determined by measuring the MB depletion over time using the following equation:

$$\text{MB uptake} = \frac{[\text{MB}_{t_0}] - [\text{MB}_{t_i}]}{[\text{MB}_{t_0}]} \times 100\%, \quad (3)$$

where $[MB_{t_0}]$ denotes the initial concentration, which is 0.5% (w/v), and $[MB_{t_i}]$ shows the concentration of MB in solution at a given time. Subsequently, samples were freeze-dried, and placed in PBS/NaN_3 to determine the MB release over time using Eq. (4):

$$\text{MB release} = \frac{[\text{MB}_{t_f}] - [\text{MB}_{t_i}]}{[\text{MB}_{t_f}]} \times 100\%, \quad (4)$$

where $[MB_{t_f}]$ denotes the final concentration. The calibration curve of MB was constructed using the absorbance value at 660 nm of MB for different concentrations (0%–0.5% w/v in PBS/NaN_3) (Fig. S1 in Supplementary Information). MB release was presented as the cumulative percent release over time. The as-prepared coatings and MB-soaked samples were photographed during analysis. Moreover, the samples (n=3) were analyzed to determine the total amount of BHT by Thermogravimetric Analysis (TGA).

Ion release profile and mechanical properties

Samples were weighed and placed in dialysis tubing (molecular weight cut-off value of 12–15 kDa) and carefully placed in a 50 mL centrifuge tube. The tube was filled with 10 mL dH_2O/NaN_3. At the end of each incubation period, all media were collected and refreshed. The collected media were diluted with 10% HNO_3 and analyzed by induced coupled optical emission spectroscopy (ICP-OES, Perkin Elmer Optima 4300DV, USA). The total release of Ca and B over 1, 7 and 14 days was determined.

The adhesive and cohesive strength of the coating was determined by a microscratch tester (n=3). The sample surfaces were scratched with a conical diamond indenter (100 μm), which was allowed to penetrate the coatings at 90°. Progressive scratching was applied at a constant rate of 4.95 N/min, starting from 50 mN to a final 3 N. The tangential force (F_T) and penetration depth (PD) were determined at the point where the tip reached the bottom Ti plate. In addition, the shelf-life of coatings was determined via measuring the change in mechanical strength over time. The samples were sterilized and placed in an aseptic cabin at room temperature under normal humidity (50%). Their mechanical strengths were determined at the end of the 4th and 8th months of storage. The as-prepared samples and stored samples were analyzed under SEM to detect the critical point at which the Ti substrate was reached during scratching, to qualitatively investigate the coating failures.

Cell proliferation study

All samples used in the cell culture studies were sterilized by dipping in 70% ethanol in dH_2O for 30 min, and then both sides were UV-irradiated for 30 min. The coatings were seeded with hFOBs at a cell density of 2×10^5, and Alamar blue assay was conducted to determine the cell proliferation on each sample. At the end of the 1st, 4th and 7th days, randomly selected samples were fixed with 4% PFA and rinsed with 0.2 M cacodylate buffer (CB). The samples were then freeze-dried for 4 h and observed under SEM.

Osteogenic and angiogenic potential

Coatings were seeded with hFOBs at a cell density of 2×10^5, and incubated for 1 day to allow complete attachment (n=6). Then, the same protocol was followed as in the HT and BHT osteogenesis study. In the qPCR analysis, additional genes such as Smad4 and BMP-2 were analyzed, whose primers are given in Table S1 (Supplementary Information). In terms of angiogenesis study, HUVECs were seeded on samples at

a density of 2.5×10^5 cells/well and allowed to adhere for 2 h in a CO_2 incubator (n=5). Samples were then incubated in EndogoXF media for 1, 4 and 7 days. At the end of each incubation period, HUVEC proliferation was determined using Alamar blue assay. At the end of the 4th day of incubation, media were collected and cells were lysed. The lysates and release media were combined in a 1:1 v/v ratio and the total VEGF-A production was quantified using a human VEGF-A ELISA kit (CSB-E11718h, Cusabio, China), which was normalized to the total DNA content. Besides, samples were randomly selected at the end of the 4th day of incubation, rinsed, fixed, and stained using the same fluorescent staining protocol as that in the cell proliferation study, to visualize cellular morphology in confocal laser scanning microscope (CLSM). The same samples were rinsed with CB, freeze-dried for 4 h, and visualized under SEM.

Immunomodulatory potential

Immunomodulatory analysis was conducted by employing a similar protocol previously elucidated in HT and BHT characterization. The THP-1s were induced with PMA, and seeded on samples at 5×10^5 cells/mL density. Randomly selected samples were further primed with LPS. All samples were tested for CAS-1 and IL-10 release after 24 h of incubation. At the same time, randomly selected samples were again either fixed and analyzed under SEM or utilized for total RNA isolation for qPCR analysis. The expression levels of NfκB, CAS-1, IL-1β, iNOS and IL-10, whose primers are given in Table S1 (Supplementary Information), were determined.

In vivo studies

All in vivo studies were approved by the Ethics Committee of Afyon Kocatepe University Experimental Animal Application and Research Center (Date: 18.09.2018, Decision No.: 49533702/147). The prepared implants (cylindrical implants with 5 mm length and 2.5 mm diameter) were sterilized by UV irradiation. The experimental rabbits were housed in normal conditions and were allowed to move, eat and drink ad libitum. Prior to the operation, the knees and femurs were shaved and antiseptic conditions were ensured. As a general anesthetic, 35 mg/kg ketamine hydrochloride and 5 mg/kg xylazin lidocaine were applied. Medial parapetellar longitudinal articulation incision was performed and the patellar medial osteochondral zone was drilled (600–700 r/min) under continuous PBS irrigation to create a 5 mm cylindrical defect. Ti-APA, A/G and A/G/BHT implants (n=4) were placed into the defect. The incision zone was stitched with Vicryl 4.0 and covered with a soft bandage. To prevent post-operative pain, rabbits were injected with Flunixin meglumin (Fynadine, Netherlands). Additionally, enrofloxacin was applied to prevent potential operational infections (Bayer, Germany). At the end of the 1st and 2nd months post-operation, a high dose of muscle relaxant was given to the rabbits to induce euthanasia. Then, femoral segments were collected and placed in formaldehyde solution (10% v/v in dH_2O) for initial fixation. After the initial fixation, the harvested femurs were placed in 4% (v/v) paraformaldehyde solution supplemented with glutaraldehyde at a final concentration of 0.1% (v/v) for 3 days. The samples were then placed under an X-ray device (TOP-X HF, Innomed, USA), and images were obtained at 45 kV and 10 mA/s to make sure that the implants were appropriately positioned (Fig. S2a in Supplementary Information). Afterward, samples were placed again in a fixative solution for an additional 7 days prior to embedding in a methacrylate resin.

Preparation of sections with intact implant-bone interface

The fixed bone samples were placed in graded glycol methacylate in dH_2O (GMA/W). Initially, samples were treated with GMA/W in 50% (v/v) for 3 h, GMA/W 70% (v/v) for 3 h, GMA/W 96% (v/v) for 3 h, and finally in 100% GMA for 6 h. While fully soaked in GMA, samples were treated with Technovit 7200/GMA mixture in a 1:1 ratio for 4 h and embedded in 100% Technovit 7200 for 36 h (Technovit 7200, Kulzer, Germany). The resin was crosslinked under UV light for 24 h. This resin provided strong bonding within the bone tissue as well as prevented heat development and implant separation from the organic tissue. While embedded in the resin, implant-bone samples were produced with precision cutting (Exakt Cutting Mill, Germany) and grinding (Exakt Micro Grinding Machine, Germany). Sections from the samples (~30 μm) were taken along the longitudinal axis from an osteochondral location toward the femur.

Masson–Goldner trichrome staining

Non-decalcified implant-bone sections were stained with Masson–Goldner trichrome using the supplier's protocol (Sigma, 1.00485.001, USA). The sections were deparaffinized with xylene, partially hydrated with reverse ethanol series (absolute to 50% in dH_2O) and fully rehydrated with dH_2O. The samples were kept in Weigert's iron hematoxylin for 5 min to dye the cell nuclei. Following rinsing under running tap water, samples were incubated in 1% (v/v) acetic acid for 30 s, placed in azofloxin for 10 min and placed again in 1% (v/v) acetic acid solution in dH_2O for 30 s. Samples were then stained with tungstophosphoric acid-Orange G solution for 1 min, rinsed in 1% acetic acid solution, subsequently stained with light green SF solution and rinsed with 1% acetic acid for 30 s to remove any unbound dyes.

Afterward, samples were dehydrated in ethanol series (50% in water to absolute grade). The ethanol was removed using xylene, and samples were embedded in Entellan mounting medium (Merck, USA). The stained samples were analyzed under light microscope (Olympus BX50) and photographed (Olympus DP25). Histochemical staining was performed, and the following results were expected: Cell nuclei were to be stained with dark brown, muscle fibers and myocyte cytoplasm to be red, erythrocytes to be bright orange, fibrous tissue to be red/pinkish, and acidic mucosal structures to be green. In addition, the obtained sections were analyzed using a method previously shown elsewhere [45]. Each section was evaluated for the criteria given in Table S3 (Supplementary Information) in four different directions (up, down, right and left from center) using ImageJ (NIH, USA).

Decalcification prior to immunohistochemical staining

In order to prevent the loss of cellular markers, samples were placed in 15% (w/v) ethylenediamine acetic acid (EDTA, pH 7.2) in dH_2O for 21 days (n=4). Every 3 days, the EDTA solution was refreshed. After incubation, samples were checked manually to observe increased elasticity, which showed the absence of Ca. Furthermore, samples were analyzed using X-ray to verify the complete removal of Ca (Fig. S2b in Supplementary Information). The decalcified sections were fully rehydrated, and 10 mM $Cu(II)SO_4$ in 50 mM NH_4Cl at pH 5 was applied 3 times for 5 min to mitigate autofluorescence. Afterward, sections were incubated in 0.5% v/v Triton X-100 for 10 min at 37 °C to retrieve the antigens. Sections were also kept in 3% v/v ImmPress HRP large spectrum kit (MP-7500, Vector Labs, USA) for endogeneous peroxidase blocking for 10 min, rinsed with PBS, and blocked in horse serum provided with the kit. These sections were dropped on a small amount of anti-OCN antibody solution (mouse monoclonal antibody OCG4, Abcam, UK) and incubated for 30 min. To develop staining, the sections were rinsed and incubated with 3,3'di-aminobenzidine (DAB) (SK-4100 DAB, Vector Labs, USA), and observed for 3 min under light microscope until the formation of a characteristic brownish color. Subsequently, sections were thoroughly rinsed and counterstained with Harris' hematoxylin, rinsed with ethanol and xylol, and covered with Entellan (Sigma, USA). The samples were visualized under light microscope (Zeiss Axio Observer Z.1 attached with Olympus DP25).

Statistical analysis

All data were given as average±standard deviation. The means of TGA data were compared to theoretical values using a one-sample t-test. All data were tested for normality. Statistical differences among groups were established by one-way ANOVA employing Tukey's Post Hoc test (*p<0.05, **p<0.01, ***p<0.001). The results of all qPCR and ELISA assays data were analyzed in pairs by an independent pairwise two-tailed t-test. The semi-quantitative scoring attributed during in vivo studies was tested for statistical difference using a Kruskal–Wallis test.

Results and discussion

Ion release and the regenerative characteristics of BHT

Studies employing B as a trace element to improve the regenerative properties of bone tissue engineering constructs have become popular [46]. Although the exact mechanism has not been deciphered, B was shown to reinforce osteogenic [47] and angiogenic [48, 49] features. However, research focusing on the effect of B as a dopant in provoking immunomodulatory response is still in its infancy. In this study, B was doped in HT, characterized to elucidate biological features, and employed in A/G coating as a multifunctional bioceramic. In our previously study [39], different compositions of BHTs were produced, and various features were characterized. It was determined that 5 mol% B containing BHT was the most effective product in terms of ion release and preliminary biological properties. Here, we elucidated the effect of BHT on regeneration and immunomodulation by interacting hFOBs, HUVECs and THP-1s with HT- or BHT-conditioned media prior to fabricating A/G/BHT composite coated Ti samples.

BHT was demonstrated to enable hFOB proliferation without showing any sign of cytotoxicity (Fig. 1a). After checking for cytocompatibility, the regenerative properties of BHT were characterized in detail. When directly compared to HT, BHT demonstrated a significant increase in ALP activity in the 2nd week (p<0.001, Fig. 1b). However, both products resulted in similar OCN release (p>0.05, Fig. 1b). Although BHT displayed a closer osteogenic protein production capacity to HT, ALP and OSX gene expressions were tremendously upregulated in hFOB after treatment with BHT (p<0.001, Fig. 1c). HT and BHT did not show any difference in terms of RUNX2 expression. Moreover, both samples induced mineralization (Fig. 1d). The strength of the staining increased from the 1st to 2nd week in correlation with CaP deposition.

There are various early and late markers that are produced and temporally monitored throughout osteoblast maturation. RUNX2 acts as a regulator of osteoblast production and is tightly controlled during the maturation of osteoblasts [50]. Additionally, long-term RUNX2 expression without a negative feedback loop triggered by osteoblasts has been shown to prevent further osteoblast differentiation [51]. In contrast,

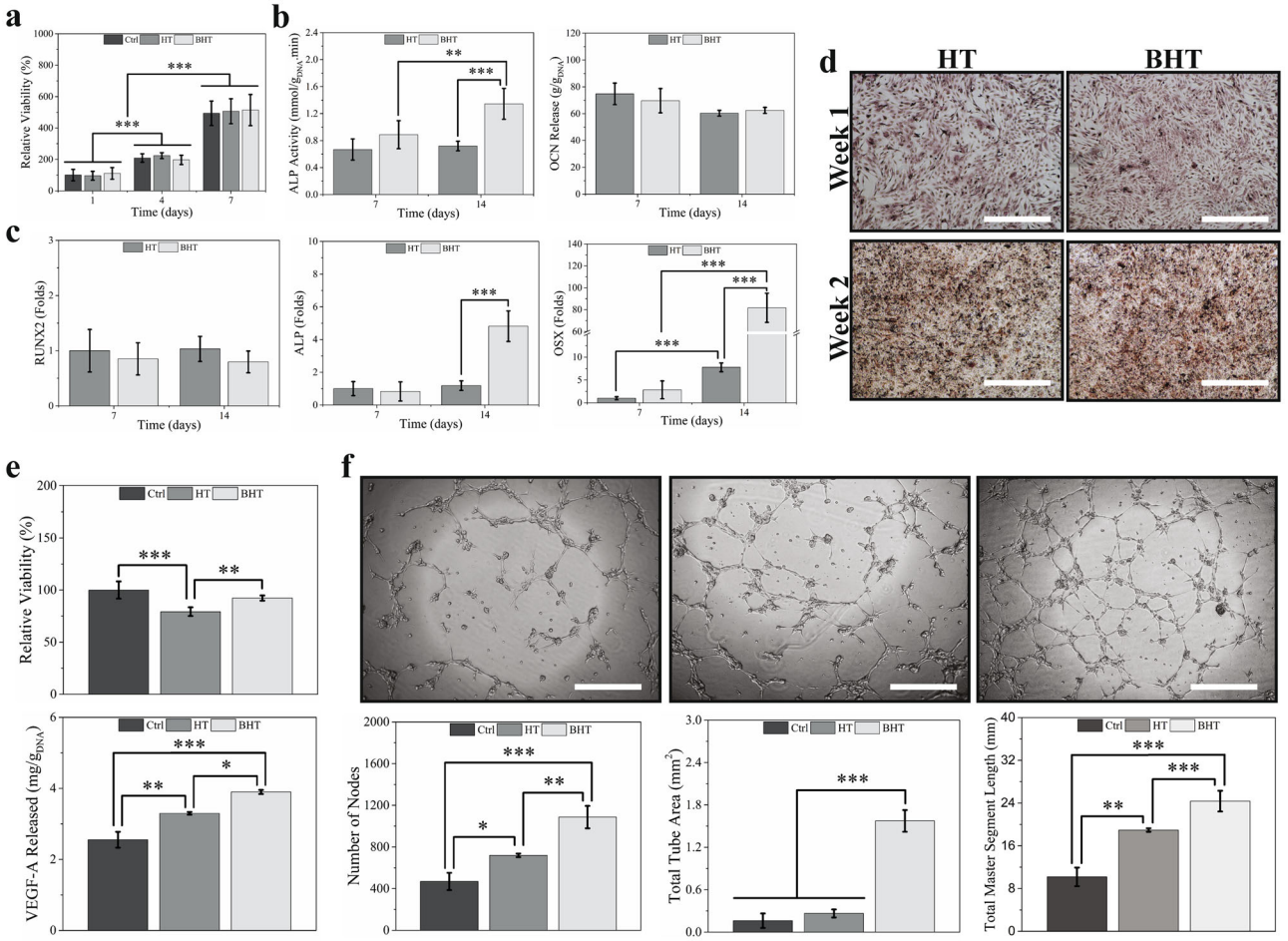

Fig. 1 Regenerative properties of HT and BHT. Relative viability (n=12, **a**), ALP (n=18) and OCN protein production (n=8, **b**), osteogenic gene expressions (n=8, **c**), and ARS staining phase contrast images (n=2, **d**) of hFOBs treated with HT- and BHT-conditioned media. BHT demonstrated significantly higher ALP activity (p<0.001); however, a comparable level of OCN release was observed. Similar RUNX2 gene expression was determined for both samples, while BHT led to statistically the highest ALP and OSX gene expressions (p<0.001). From a qualitative aspect, HT and BHT showed analogous ARS staining (**d**). HUVEC relative viability and VEGF-A release, and the angiogenic tube formation characteristics of HUVECs after treatment with HT- and BHT-conditioned media (**e**). BHT showed good HUVEC viability (n=6) and prompted the highest VEGF-A release (n=4, p<0.001 vs. Ctrl and p<0.05 vs. HT). Phase contrast images (**f**) of HUVECs on Matrigel while treated with HT- and BHT-conditioned media were used to quantify the tube formation parameters, wherein BHT excelled in comparison with Ctrl and HT (p<0.001). Statistical differences were given as *p<0.05, **p<0.01 and ***p<0.001. Scale bars in **d** and **f** are 500 μm

Table 2 Release of Ca and B from HT and BHT (n=3)

Sample	Week 1		Week 2	
	Ca (mg/L)	B (mg/L)	Ca (mg/L)	B (mg/L)
HT	62±4	0	128±5	0
BHT	36±5	39±12	66±5	52±14

HT showed the highest Ca release, while only BHT showed B release

ALP was reported to peak during osteoblast differentiation toward osteocytes [52] and is maintained throughout osteoblast-osteocyte transition to allow for biomineralization. BHT induced a clear increase in ALP production and expression, but RUNX2 expression did not change over time. Meanwhile, the release of OCN to ECM and the expression of OSX surged. Following the initiation of CaP deposition, the OCN production, release and its binding to organophosphate residues increased immediately [53]. At the same time, another late marker, OSX, was upregulated to drive the osteoblast to osteocyte phenotypic differentiation and ECM maturation [54]. Owing to the increased OSX fold change upon BHT induction in comparison to HT, it could be pointed out that hFOBs under the BHT stimulation demonstrated clearly improved osteoblast maturation. As shown in Table 2, in spite of the drastically lower Ca release, BHT led to high B release and reinforced osteogenic properties of HT. Therefore, it could be projected that B, similar to Ca, possesses osteogenic potential and may promote higher ALP and OCN production and OSX expression.

Prior to the VEGF-A release and tube formation study, samples were tested for HUVEC viability. No cytotoxicity was observed in any of the samples; however, HT-treated HUVECs exhibited the lowest viability ($p<0.001$ vs. Ctrl and $p<0.01$ vs. BHT, Fig. 1e). BHT-treated HUVECs released the highest concentration of VEGF-A ($p<0.001$ vs. Ctrl and $p<0.05$ vs. BHT, Fig. 1e). At the same time, HT prompted higher VEGF-A release compared to Ctrl ($p<0.01$). Furthermore, angiogenic response in the form of vessel-like tube growth and evolution on Matrigel in the presence of HT- and BHT-conditioned media was analyzed (Fig. 1f). BHT drastically increased node formation ($p<0.01$ vs. HT and $p<0.001$ vs. Ctrl), master segment length ($p<0.001$), and increased total mesh area ($p<0.001$).

As expected, BHT supported rapid tube formation and triggered the greatest VEGF-A release in comparison to the HT counterpart. B was shown to induce angiogenic response when employed in various forms [55], which directly partakes in VEGF-A release [56] and tube formation [57]. VEGF-A is an important regulator of angiogenesis and osteogenesis [58]. Especially exerting its role in endochondral ossification (EO), VEGF-A could support the healing-repair process at the bone defect site as well as allow for establishing a functional bridge between bone and implant [59]. In agreement with the literature data, B was proven to critically improve the angiogenic potential of HT bioceramic.

Immunomodulatory characteristics of BHT

Besides possessing regenerative ability, new-generation bioceramics have been produced that also present multifunctionality. Here, we tested BHT against HT in terms of immunomodulatory properties, to determine whether B as a dopant endowed versatility to HT. Initially, THP-1s were incubated in HT- and BHT-conditioned media and no cytotoxicity was observed (Fig. 2a). Then, the levels of three important proteins involved in the inflammatory answer to biomaterials were quantitated (Fig. 2b). The results for total CAS-1 protein revealed that HT or BHT did not incite pyroptosis as much as the LPS-triggered response (LPS-primed PMA-differentiated THP-1s, $p<0.001$). Nonetheless, BHT did not increase CAS-1 as it did not have a significantly higher value; however, HT brought about higher CAS-1 production ($p>0.05$ vs. BHT, $p<0.01$ vs. PMA). A similar trend was observed to be at play for iNOS production. HT-treated THP-1s produced higher iNOS than BHT despite lacking a statistical difference. On the other hand, BHT led to significantly lower amount of iNOS produced in comparison with PMA ($p<0.05$). Moreover, BHT led to higher IL-10 production compared to HT, though no statistical difference was detected. In comparison with PMA, significantly lower IL-10 production was reached by HT-treated THP-1s ($p<0.05$). These cells also showed similar IL-10 with PMA + LPS. However, BHT generated a more positive response, in that higher IL-10 production was observed when compared to PMA + LPS ($p<0.01$). The IL-10 production of THPs after incubation in BHT-conditioned media was also close to that of PMA.

The release of CAS-1 signals a strong inflammatory response that could provoke pyroptosis, thus a prolonged inflammation may occur [60]. Subsequent to the viability assay, CAS-1 protein quantitation was conducted to confirm that none of the samples drive THP-1s to chronic inflammation. After observing no drastic increase in the CAS-1 production by BHT, we further went on to iNOS and IL-10 quantitation. Because the timed resolution of inflammation could prompt a pro-healing cascade, it may thus improve the rate of implant integration. Although iNOS and IL-10 mark two opposite sides of the immune response spectrum to a stimulus (anti- or pro-healing, respectively), they are released by both M1- and M2-type macrophages and expected to be in balance [61].

As observed in Figs. 2c and 2d, both samples led to rounder THP-1s than those with spindle morphology. Moreover, BHT generated a vibrant environment with a higher number of spindle-like cells than HT; therefore, it can be suggested that BHT presence could allow for rapid macrophage colonization and may prevent chronic inflammation. As reported by Dollinger et al. [62], the cytoplasm becomes larger, and cells turn into ones with more ruffled and round morphology as M1s persist in the colony. Hence, BHT is expected to lead a lenient immunological response in comparison to HT.

Collectively, BHT induced lower CAS-1 and iNOS production but higher IL-10, indicating that BHT possesses more potential to alleviate the inflammatory response in comparison to HT. THP-1s assumed spindle-like morphology and

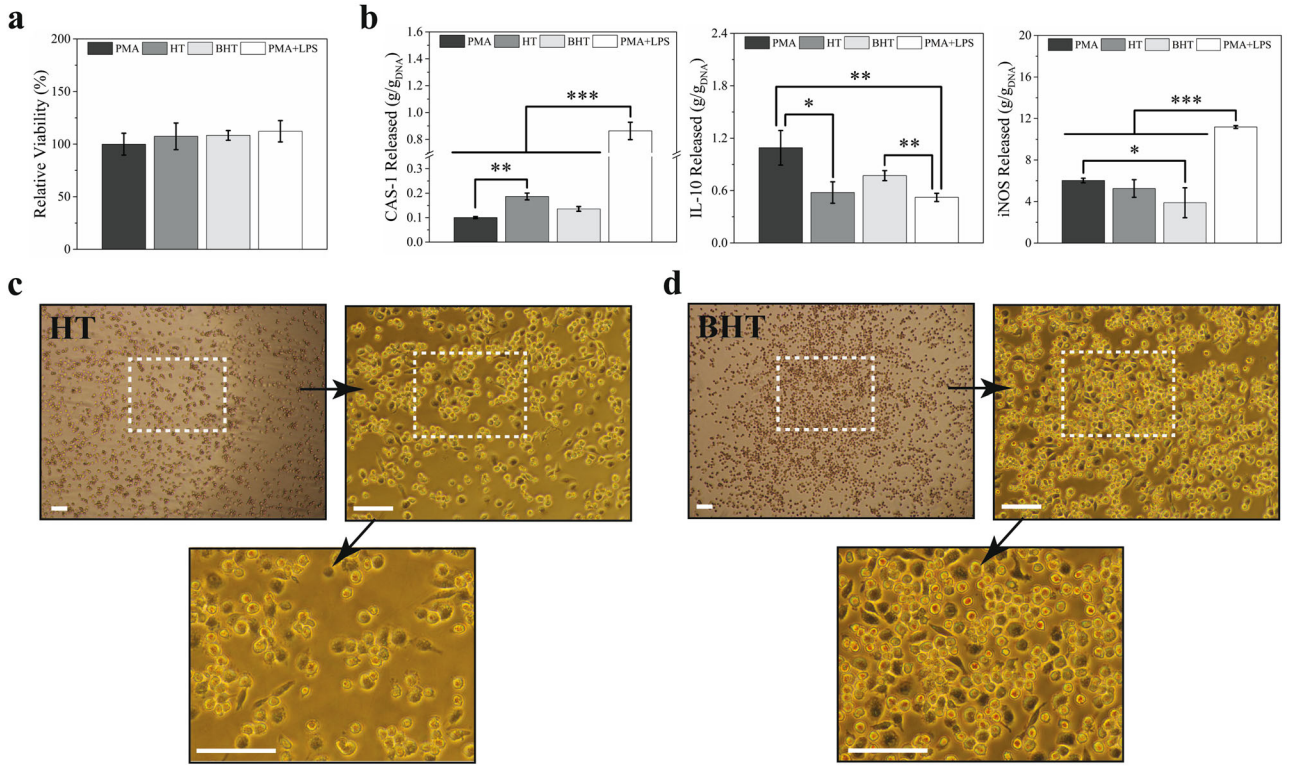

Fig. 2 THP-1 relative viability (n=4, **a**), CAS-1, iNOS and IL-10 inflammation-related protein production (n=4, **b**); the morphological response of THP-1s to HT (**c**) and BHT (**d**) after treatment with conditioned media. None of the samples were cytotoxic to THP-1s. The BHT revealed good immunomodulatory response, since it alleviated CAS-1 and iNOS production and prompted higher IL-10 production compared to HT. BHT also promoted a highly responsive microenvironment for THP-1s with high number of spindle-like morphology, which indicates good immunomodulation by BHT. Statistical differences were given as *p<0.05, **p<0.01 and ***p<0.001. Scale bars in **c** and **d** are 50 μm

demonstrated a dynamic nature when treated with BHT. Therefore, it can be interpreted that BHT could attenuate the inflammatory cascade and may support osseointegration through immunomodulation.

Design considerations, and the rheological, physical and chemical features of coatings

In our previous study, we designed a non-delaminating, strong and highly competent A/G layer on Ti-APA and demonstrated its 12-month-long shelf-life and ability to burst release a charged MB model drug [38]. Here, we aimed to establish a cohesive composite matrix possessing ECM-like features, which could be readily swollen upon contact with blood, thus transforming into a hydrogel that could release both regenerative and immunomodulatory cargo. This composite layer was realized with BHT loaded into an A/G hydrogel, coated on the Ti-APA surface and stably freeze-dried. As observed in Fig. 3a, pliable and crack-free composite coatings were obtained. We further established that A/G/10BHT was conformed on medical Ti screws and pins (Fig. 3b). Thus, it was concluded that the method is also applicable to irregularly shaped surfaces. Moreover, A/G and A/G/BHT coatings were analyzed for MB loading/release and qualitatively tested for B release from the surface (Figs. 3c and 3d). Dried samples were placed in the MB solution and it was observed that both coatings took MB up fully and rapidly released the dye (Figs. 3c and 3f). With the ability to be loaded with a charged drug such as MB, a good burst release ability of A/G and A/G/BHT layers was demonstrated. In addition, samples were wetted and placed in a Carmine dye solution. Because this dye specifically darkens over time in relation to B presence [63], we determined that the A/G/BHT layer could release B ions to the environment within 15 min after initial wetting (Fig. 3d).

Upon microscopic examination, the A/G layer was shown to appear seamless and without bulges or cracks (Fig. 3e). In contrast, the BHT inclusion transformed the whole surface in favor of highly rough topography; separate BHT particles were observed within the A/G hydrogel layer rather than agglomerates. This could be the result of 0.2 M NaCl addition into the pre-gel solution. In our previous study, we employed NaCl to decrease the viscosity, so as to achieve a homogeneously coated layer. Herein, NaCl addition also ceased the

gelation of A/G once BHT was added (Fig. S1 in Supplementary Information). In a study by Su et al. [64], Na^+ was observed to compete against Ca^{2+} to interact with negatively charged carboxylic units; however, being a monovalent ion, Na^+ was not able to induce gelation and prevented Ca^{2+} to interact with alginate chains. They also showed that NaCl allowed for improved protein diffusion in alginate beads by decreasing the ionic interactions between chains while inducing extensive hydrogen bonding.

In line with the aforementioned studies, low-viscosity pre-gel was obtained (Fig. 3f). As its shear rate was increased, its viscosity decreased very rapidly, quickly reaching a plateau. It was also very interesting to see that the presence of 5% or 10% w/v BHT did not cause a drastic change in viscosity under shear stress. As reported by Narayanan et al. [65], a thicker and highly cohesive hydrogel layer is very hard to adhere on a surface due to intramolecularly favored gelation. Therefore, by obtaining a shear thinning solution, we were able to homogeneously mix BHT particles at as high as 10% w/w and thoroughly coated the implant surfaces. In addition, the implant surface was coated with a thin alginate layer to effectively accommodate upcoming A/G or A/G/BHT layers. To overcome the flow of pre-gel on implants, we employed an alginate layer to increase the surface tackiness, thus obtaining a homogeneously thick composite hydrogel layer on the surface [66].

TGA analysis revealed that the experimental BHT content was close to the theoretical value (Fig. 3g). However, A/G/10BHT was observed to have statistically higher BHT content ($p<0.05$). This could be the result of NaCl moieties left in the hydrogel, as they might not have been thoroughly removed by rinsing. Furthermore, it is of high importance to note that BHT comprises 56% w/w of A/G/5BHT and 70% w/w of A/G/10BHT in their final dry forms.

The effect of high BHT content was manifested in terms of water uptake ability and hydrolytic degradation rate (Figs. 3h and 3i). Bare A/G coatings resulted in the highest water uptake of (977±45)% ($p<0.001$) as early as 24 h, and then leveled off. Similarly, A/G/BHTs peaked at the end of the 24-h period. However, increasing the BHT content from 5% to 10% led to a drastic decrease in swelling ability ($p<0.001$). A/G/5BHT swelled up to (580±45)% and A/G/10BHT showed (362±45)% increase in weight. Therefore, it can be speculated that the inclusion of BHT did not bring about a plasticizer effect, but rather it enabled the compaction of alginate and gelatin chains due to the release of Ca and B. However, it was determined that MB was loaded as fast as 3 h and released within 15 min of the initial wetting (Figs. 3j and 3k). This demonstrates the critical ability of A/G/10BHT coatings that neither the presence of BHT affected drug loading rate nor it showed any effect on the release profile. Ratanavaraporn et al. [67] demonstrated that the alginate/gelatin/hyaluronic acid hydrogel system performed considerably well owing to the burst release of antibiotic drugs to rapidly eliminate bacterial infection. In addition, Jing et al. [68] showed that an alginate/chitosan-based hydrogel was able to collect exudate at the defect area due to its rapid swelling capacity. Therefore, it is possible for our coatings to stabilize the wound area while triggering drug release to modulate host-implant interaction.

Recently, coatings have been designed using natural polymers to undergo homogeneous hydrolytic/enzymatic erosion for proportionate dissociation [69]. This concept plays a pivotal role in designing suitable coatings showing good overall stability and the controllable release of their cargo over time. In this sense, we determined that A/G coatings hydrolytically degraded much faster than BHT-loaded counterparts (Fig. 3i). Although no statistical difference was observed between A/G and A/G/5BHT, A/G/10BHT demonstrated significantly lower weight loss in 4 weeks compared to A/G ($p<0.001$). The reduction in degradation rate with the increase in BHT content was also noted.

Ion release profile and mechanical properties of coatings

We observed that the structural, topographical, physical and chemical properties were substantially improved and the rheological properties did not change with the increase of BHT concentration. Therefore, the further investigation of the effect of BHT inclusion in A/G was pursued by using the 10BHT counterpart. From this point on, A/G/10BHT will represent A/G/BHT.

The ion release study revealed that A/G/BHT samples released the highest amount of Ca compared to A/G ($p<0.001$, Table 3). This trend continued until the end of the study. In terms of B, A/G/BHT was shown to release a lower rate of B in comparison to unloaded BHTs (Table 3). Since BHT was in a hydrogel structure, Ca and B could be entrapped, and they might also partake in ionic interactions with the polymer chains. Nonetheless, A/G/BHT allowed the release of multifunctional Ca and B ions throughout the experiments.

A microscratch analysis was conducted to quantitate the total mechanical strength of coatings as a sum of adhesiveness and cohesiveness (Table 4, Fig. 4a). The utilization of BHTs in a composite coating structure tremendously enhanced coating adhesion to the implant surface ($p<0.001$). The increment in tangential force (F_T) increased with BHT inclusion (Table 4, Fig. 4b). In addition, the strength of coatings decreased over time for both samples. A/G was observed to possess 1/3 of its original strength, while A/G/BHT maintained more than half of its original strength at the end of the 8-month storage period. Moreover, similar PDs were obtained for all samples (Table 4). Although a slight increase in the thickness of coatings was detected over time during

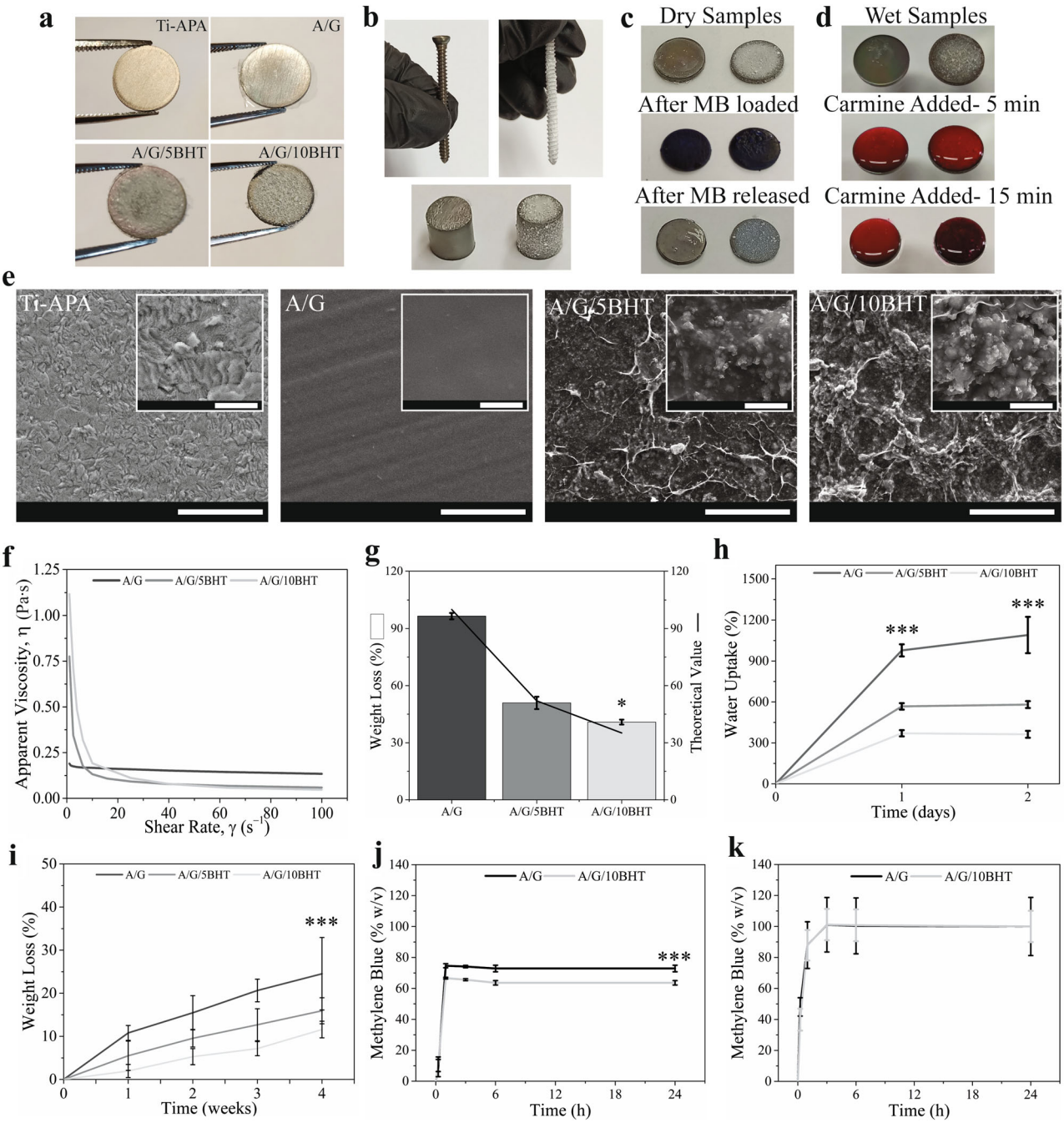

Fig. 3 Macroscopic images of samples (**a**), A/G/10BHT-coated screw and pin (**b**), MB study (**c**) and carmine staining (**d**). Microscopic images (**e**), apparent viscosity measurement (**f**), TGA analysis (**g**), water uptake (**h**), hydrolytic degradation studies (**i**), and the MB loading-release (**j**, **k**) analysis of coatings. For **f** duplicate measurements were obtained, while **g**–**k** had n=4. The scale bar in **e** is 100 μm and the inset scale bar is 20 μm. In **h**–**j**, A/G showed statistically higher values than A/G/10BHT (p<0.001). In **b**–**d**, A/G and A/G/10BHT were selected as representative samples. Statistical differences were given as *p<0.05, **p<0.01 and ***p<0.001

Table 3 Cumulative release of Ca and B from A/G and A/G/BHT (n=3)

Sample	Day 1		Day 7		Day 14	
	Ca (mg/L)	B (mg/L)	Ca (mg/L)	B (mg/L)	Ca (mg/L)	B (mg/L)
A/G	7.4±0.1	0	45.3±1.04	0	84.4±3.2	0
A/G/BHT	96±2	0.41±0.1	251±3	1.1±0.2	286±3.6	1.53±0.2

HT showed the highest Ca release, while only BHT showed the release of B

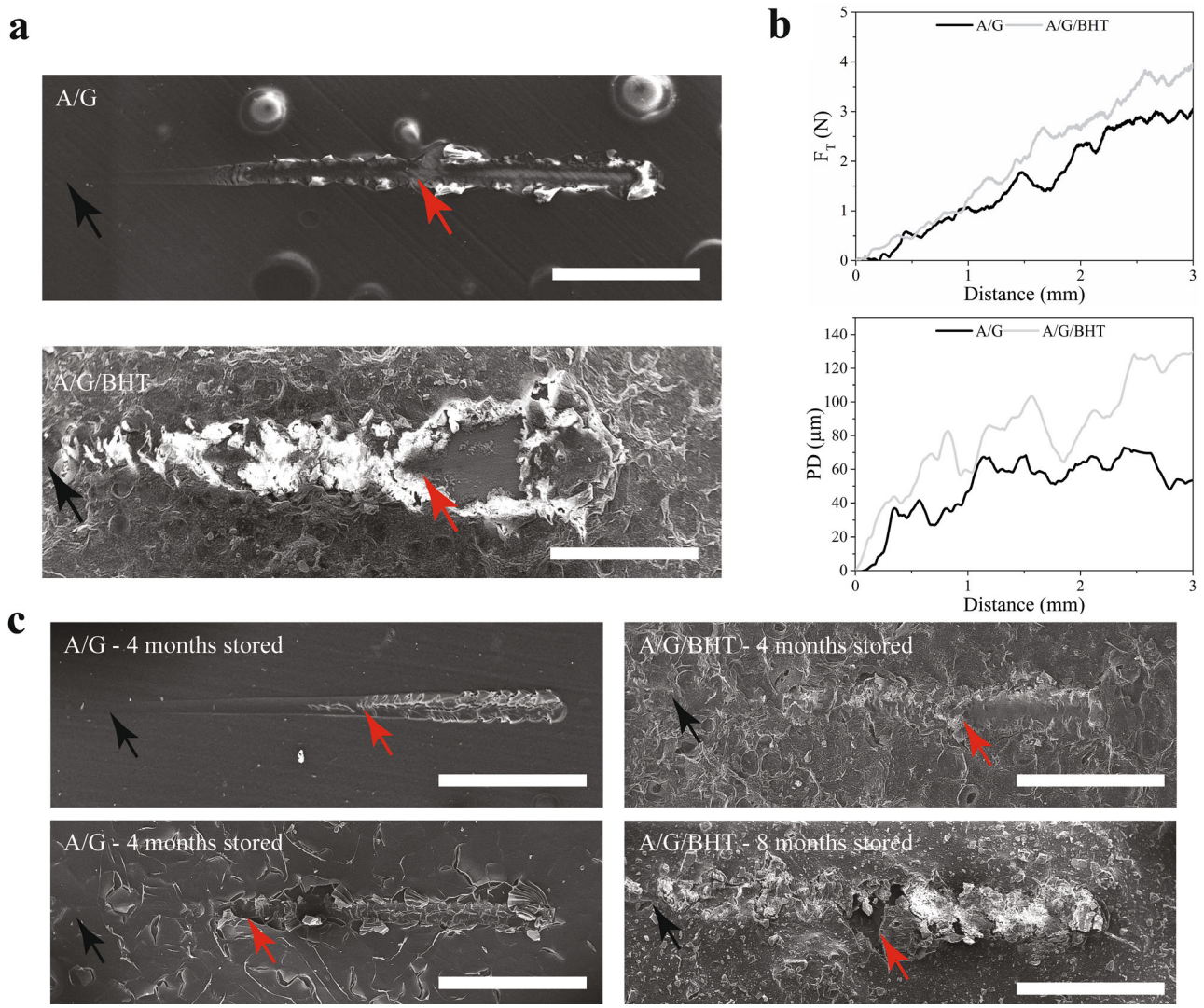

Fig. 4 SEM images of scratches obtained during coating strength analysis. Scratched samples after production (as-prepared, **a**), change in F_T and PD during microscratch analysis (**b**), and images of the resultant surfaces during shelf-life analysis (**c**). The black arrows indicate the starting point of scratching and the red arrows show the point where the tip reached the bottom surface. Scale bars: 1 mm

Table 4 Microscratch results of A/G and A/G/BHT (n=3)

Samples		F_T (N)	PD (μm)
As is	A/G	1.72±0.11	57.74±13.39
	A/G/BHT	2.66±0.10***	68.85±13.84
4-month storage	A/G	1.32±0.19	63.73±2.68
	A/G/BHT	2.48±0.07***	69.27±4.47
8-month storage	A/G	0.63±0.04	65.25±17.48
	A/G/BHT	1.78±0.25***	89.80±1.65

***A/G/BHT demonstrated significantly higher adhesive strength

storage, no abrupt increase in thickness or sudden structural fail was detected.

The scratch paths were inspected to determine the type of failures observed on various composite coatings (Figs. 4a and 4c). Similar to the findings acquired during the microscratch analysis of A/G coatings, cohesive failure was observed for all samples. From the start point (black arrows) up until the end point (red arrows), no delamination or cracking occurred beyond the scratch path for all samples. Moreover, the presence of BHT affirmed that coating strength was exceptionally improved; thus, a break in the coatings was observed at a later point on the A/G/BHT samples. Furthermore, no delamination or cracking was observed during shelf-life analysis (Fig. 4c). All of the samples remained intact for 8 months at room temperature.

According to the previously elucidated structural, physical and chemical properties, the coatings demonstrated improved mechanical properties as well as the ability to burst release charged drugs (MB dye) and provide the controlled release of multifunctional Ca and B ions while maintaining structural coherence for at least 8 months. Zhang et al. [70] demonstrated the presence of high Ca in alginate-based hydrogels, which not only allowed for a highly elastic and cohesive structure but also enabled Ca to endow self-healing and high adhesiveness properties to the ALG matrix. The positive effect brought about by the presence of BHT in the A/G matrix could be the result of having high Ca ions around polymer chains and BHT particles electrostatically keeping the chains in close proximity, thereby increasing cohesive strength.

Regenerative properties of coatings

For this experiment, human fetal osteoblasts were seeded on the samples, and cell proliferation was analyzed on various coatings (Fig. 5a). It was observed that both A/G and A/G/BHT coatings improved hFOB attachment and significantly increased (p<0.001) the rate of hFOB proliferation over 7 days. The A/G coatings resulted in higher cell growth than Ti-APA (p<0.001), possibly as a result of having cell recognition and attachment patterns owing to the presence of gelatin [71]. As reported by Stubbe et al. [72], alginate has been mostly utilized along with gelatin to prevent cell loss due to low cell attachment on pure alginate. In spite of its biocompatibility, alginate is highly anionic and especially repels osteoblasts since their surface is negatively charged. Therefore, inclusion in gelatin not only provides cell adhesive peptide sequences but also neutralizes the surface charge. Additionally, due to its surface roughness, A/G/BHT might have resulted in the highest relative cellular growth (p<0.001). Taken together, the results signify that coatings successfully improved the ability of osteoblasts to attach and flourish on A/G/BHT.

Cells on different surfaces attached independently of each other, not forming any clusters and demonstrating spindle-like morphology (Figs. 5b and 5c). They were observed to proliferate and colonize all surfaces effectively; however, they were in a monolayer on Ti-APA (Fig. 5b). Meanwhile, both on A/G and A/G/BHT, hFOBs were in multilayers. Moreover, hFOBs on these groups were determined to have lamellopodia and spread much more than Ti-APA, as seen in the SEM images (Fig. 5c). Therefore, our cell proliferation study proved that A/G/BHT coatings could indeed provide a suitable substrate for cell growth and colonization.

The osteogenic capacity of hFOBs incubated on various samples directly demonstrated the osteoinductivity potential of these surfaces. A/G/BHT showed significantly higher ALP activity at the end of the 1st week in comparison to Ti-APA (p<0.05, Fig. 6a). Similarly, OCN release was observed to be the highest in hFOBs incubated on A/G/BHT, but with no statistical difference (Fig. 6a). In the 2nd week, ALP activity as well as the concentration of OCN released to the extracellular medium peaked for all samples. A/G/BHT led to the highest ALP activity (p<0.001), while A/G triggered greater ALP activity compared to Ti-APA alone (p<0.01). This trend was also observed for OCN release in that A/G/BHT demonstrated the highest concentration despite lacking statistical difference compared to Ti-APA or A/G. OCN was studied as the late osteogenic marker taking a direct part in biomineralization, similar to the ALP enzyme [73]. Following the initiation of calcium phosphate deposition in the ECM, OCN production, release and its binding to organophosphate residues immediately increase [53]. Therefore, we could observe an increase in the late marker OCN release while intracellular ALP activity persisted. Despite the higher OCN release obtained for A/G/BHT in the 1st week, no statistical difference was detected between the samples (Fig. 6a). An analogous situation was also found for the 2nd week results. Hence, A/G/BHT appeared to induce strong hFOB mineralization.

In order to evaluate the overall osteogenic response at the transcriptional level, qPCR for specific genes was performed (Fig. 6b). It was expected from osteogenic surfaces

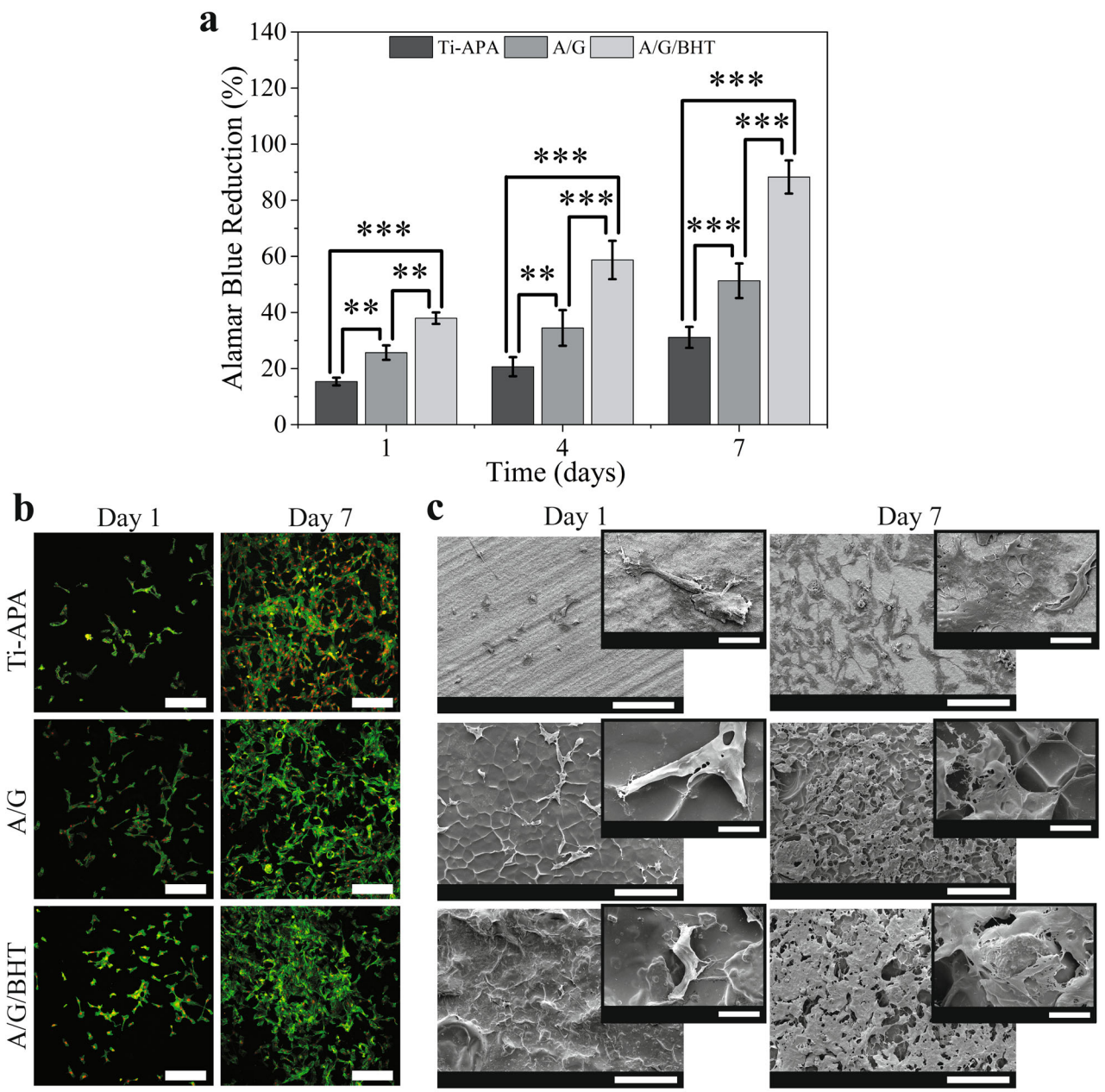

Fig. 5 Cell proliferation assay (n=5, **a**), and images of cells on various coatings at different time points, as obtained by CLSM (**b**) and SEM (**c**). The scale bar of CLSM is 450 μm, the scale bar of SEM is 200 μm and the inset bar is 20 μm. Statistical differences were given as *p<0.05, **p<0.01 and ***p<0.001

that they would induce cells used as osteoblast models, such as hFOBs, to expand in number, differentiate toward a mature osteoblast phenotype and finally become osteocytes. Cells incubated on A/G/BHT revealed a clear increment in the expression of late osteogenic markers, while a steep decline in Smad4 and RUNX2 was observed over time (Fig. 6b). A/G/BHT led to a higher expression of Smad4 after incubation for a week, as compared to A/G and Ti-APA (p<0.001). This trend completely reversed by the 2nd week of incubation, albeit without a significant difference between samples, and it was displayed that Smad4 expression peaked in the 1st week of analysis for the cells incubated on A/G/BHT. In parallel, it was observed that RUNX2 was the highest for hFOBs incubated on A/G/BHT, although there was no statistical difference. On the contrary, A/G/BHT prompted a lower RUNX2 expression in comparison with other samples by the

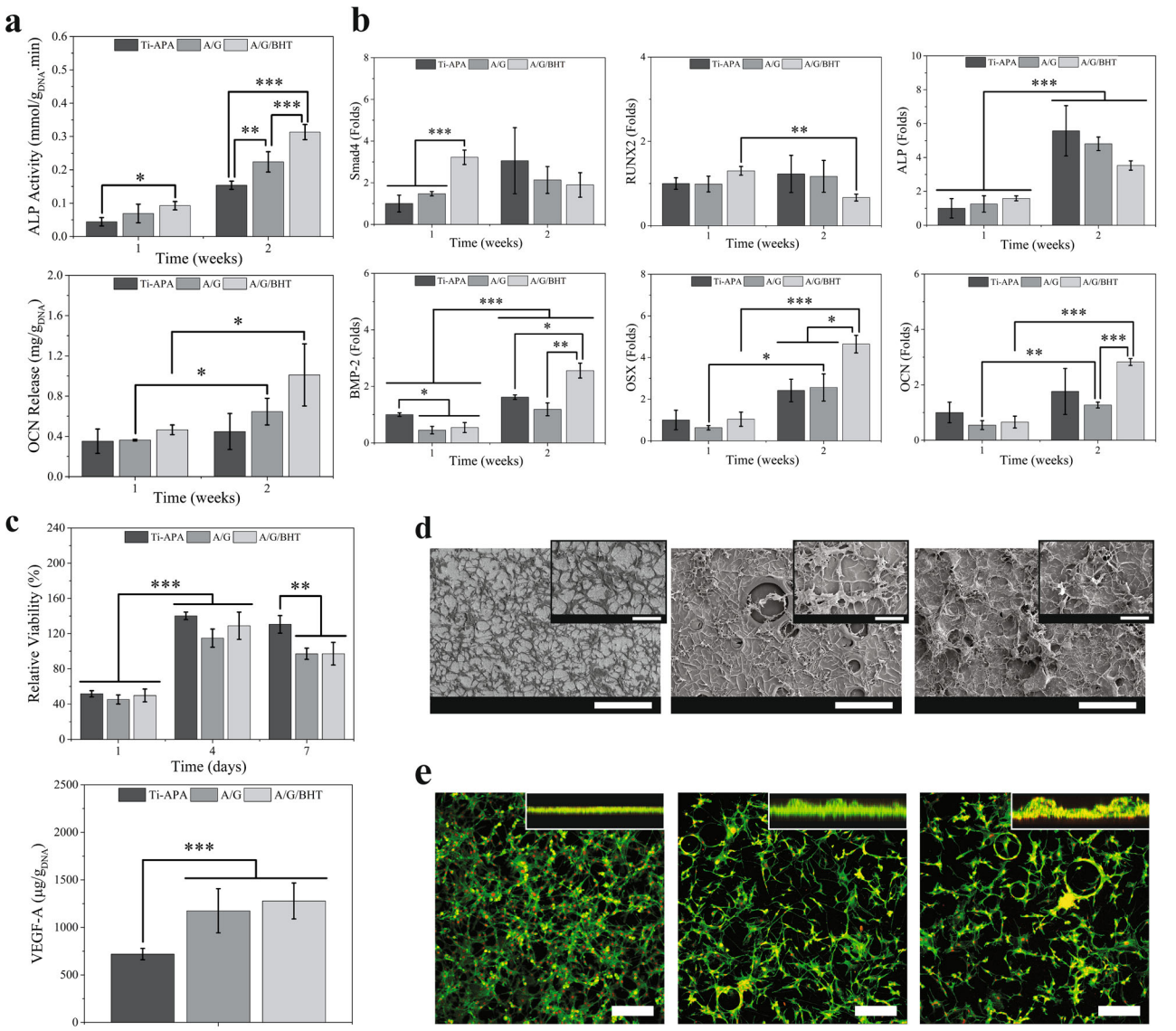

Fig. 6 Regenerative properties of coatings in terms of osteogenesis and angiogenesis. ALP activity (duplicate study with n=4) and OCN release (n=4, **a**), and the early and late osteogenic gene expressions (duplicate study with n=3, **b**) of hFOBs. Cells incubated on A/G/BHT clearly demonstrated more rapid osteogenic differentiation, as observed by the highest ALP activity, OCN release and overall increase in expression of late osteogenic markers such as BMP-2, OSX and OCN. HUVEC relative viability and VEGF-A release at the end of the 4th day of incubation (n=5, **c**), the SEM (**d**) and CLSM (**e**) images of HUVECs on various coatings. VEGF-A release was quantitated on the 4th day due to having the highest HUVEC number on coatings. A/G/BHT exhibited good angiogenic potential and acted as a suitable substrate for endothelial growth and differentiation. The scale bars of SEM images are 300 μm, the inset bars are 100 μm, and the bars of CLSM images are 450 μm. Statistical differences were given as *p<0.05, **p<0.01 and ***p<0.001

end of the 2nd week. The expression analysis of another early marker, the ALP gene, demonstrated statistically insignificant differences among the samples at the end of both the 1st and 2nd weeks. However, two points should be noted in this context: A/G/BHT allowed for a more rapid increase in ALP expression by the end of the 1st week, and all samples led to a tremendous increase in ALP expression (p<0.001). Therefore, it is thought that hFOBs matured more efficiently on A/G/BHT, and osteoblast differentiation was achieved more rapidly.

Upon determining the expression levels of late osteogenic marker genes, it was observed that osteoblast maturation was indeed at play and rapid osteogenesis was promoted on A/G/BHT. Three genes, BMP-2, OSX and OCN, all demonstrated the highest fold change for A/G/BHT (Fig. 6b).

These cells upregulated OSX tremendously higher compared to A/G and Ti-APA ($p<0.01$ and $p<0.05$, respectively). This trend ensued for BMP-2 expression ($p<0.05$), while OCN expression demonstrated similar results for Ti-APA and A/G/BHT ($p>0.05$). Nonetheless, A/G/BHT revealed a significant increase in OSX and OCN expression compared to the other samples over time ($p<0.001$). Interestingly, Ti-APA performed better compared to A/G with regards to the increase in osteogenic marker expression, despite the lack of statistical difference.

Owing to being an important canonical gene taking part in cell proliferation and differentiation, Smad4 was found to be highly expressed in osteoblast maturation [74]. As previously mentioned, RUNX2 also takes part in the early maturation of osteoblasts, while ALP expression is maintained throughout the differentiation process until osteocyte formation. Moreover, BMP-2 is involved in osteogenic differentiation through collagen mineralization and suppressing osteoclastogenesis [75], along with OSX. It was observed that these markers were enhanced in A/G/BHT coatings. In addition, it was reported that the commitment of cells to osteoblast differentiation was marked by an early increase in Smad4 and its direct involvement in RUNX2 expression [76]. In addition, this early increase was followed by higher expressions of OCN, BMP-2 and OSX, revealing that hFOBs were prompted to undergo phenotypic change.

Our osteogenesis study revealed that the A/G/BHT coating was the most osteogenic surface. The previously demonstrated mechanical and physical properties of A/G/BHT led to the formation of a highly cohesive layer, which in return provided a stiffer substrate in comparison with A/G. Ti-APA has been previously employed as a standard implant preparation method, because the APA modification brings about an increment in osteogenic genes involved in osteoblast maturation through mechanobiological pathways due to enhanced roughness and stiffness [77, 78]. However, it was discussed elsewhere that a mechanobiological trigger itself is insufficient to successfully drive osteoblastogenic differentiation [79, 80]. Parallel to these findings, the initial strong response of hFOBs toward the Ti-APA surface was evident, as it generated a more prominent BMP-2 and OCN expression compared to A/G. Subsequently, this surge was surpassed by A/G/BHT (Figs. 6a and 6b). Since osteogenic ion release (Ca and B) and rapid cell proliferation were prompted by A/G/BHT owing to ECM-like features, hFOBs differentiated to a mature phenotype faster. Therefore, it can be concluded that hFOBs acted in response to the sum of structural properties, surface topography, ECM-like chemical make-up and osteogenic ion release. In return, chemical and biological factors reinforced by the presence of BHT were shown to play a rather essential role in driving hFOB differentiation on A/G/BHT.

In addition to osteogenesis, angiogenic response plays a critical role in governing a healthy response to bone damage when an implant is placed. Moreover, it is a key to provide a functional bridge between the bone and the metal surface. Endothelial proliferation and the development of vascular tissue could allow nutrient flow, the continuous exchange of gases, the removal of waste and maintaining the pH of ECM; thus, it may reinforce bone growth over the implant surface and achieve a robust bone-implant fusion [81]. Here, HUVECs were employed as model cells capable of inducing an angiogenic response [82]. It was observed that cells could attach to and proliferate on all samples (Figs. 6c and 6d). Ti-APA resulted in the highest cell viability on day 7, while other samples demonstrated a decline ($p<0.01$). The highest HUVEC viability on all samples was observed to be at the end of the 4th day. Hence, the quantification of VEGF-A release via ELISA was opted for on the 4th day of incubation [83]. We observed that both A/G and A/G/BHT yielded a similar release of VEGF-A; however, Ti-APA triggered significantly lower release ($p<0.001$, Fig. 6c). In terms of morphological analysis, HUVECs on all samples demonstrated similar morphology with a great number of intercellular connections and spreading throughout the surface (Fig. 6d). HUVECs on Ti-APA showed spread morphology, whereas they did not form any colonies. In comparison, A/G and A/G/BHT harbored cell groups in more colony-like formations (Fig. 6e). As reported previously, in a 3D confinement or on a structure that could be easily colonized, HUVECs tend to form small multilayered colonies and migrate to establish tubular structures [84]. In return, tubular structures demonstrate the capability of surface structure—A/G/BHT in this case—to be more receptive to vascularization.

In a study by Li et al. [85], a combination of alginate with gelatin as a bioink system was manufactured, and it was shown that gelatin presence drastically enhanced cell adhesion and migration. They further highlighted the fact that the spatial distribution of cells and morphological response to surface properties were also responsible for driving phenotypic change. Therefore, we speculated that, in addition to various factors prompting osteogenesis and angiogenesis, cellular differentiation may indeed be linked to rapid colonization and growth on implant surfaces.

Immunomodulatory properties of coatings

THP-1s seeded on Ti-APA, A/G and A/G/BHT under various conditions revealed that A/G and A/G/BHT coatings led to a small decrease in cell viability from approximately 40% to 30%, while Ti-APA significantly hampered cell viability, showing a steep decline from 60% to 34% (Fig. 7a). Interestingly, Ti-APA allowed for the highest THP-1 colonization without LPS priming ($p<0.01$), while coatings

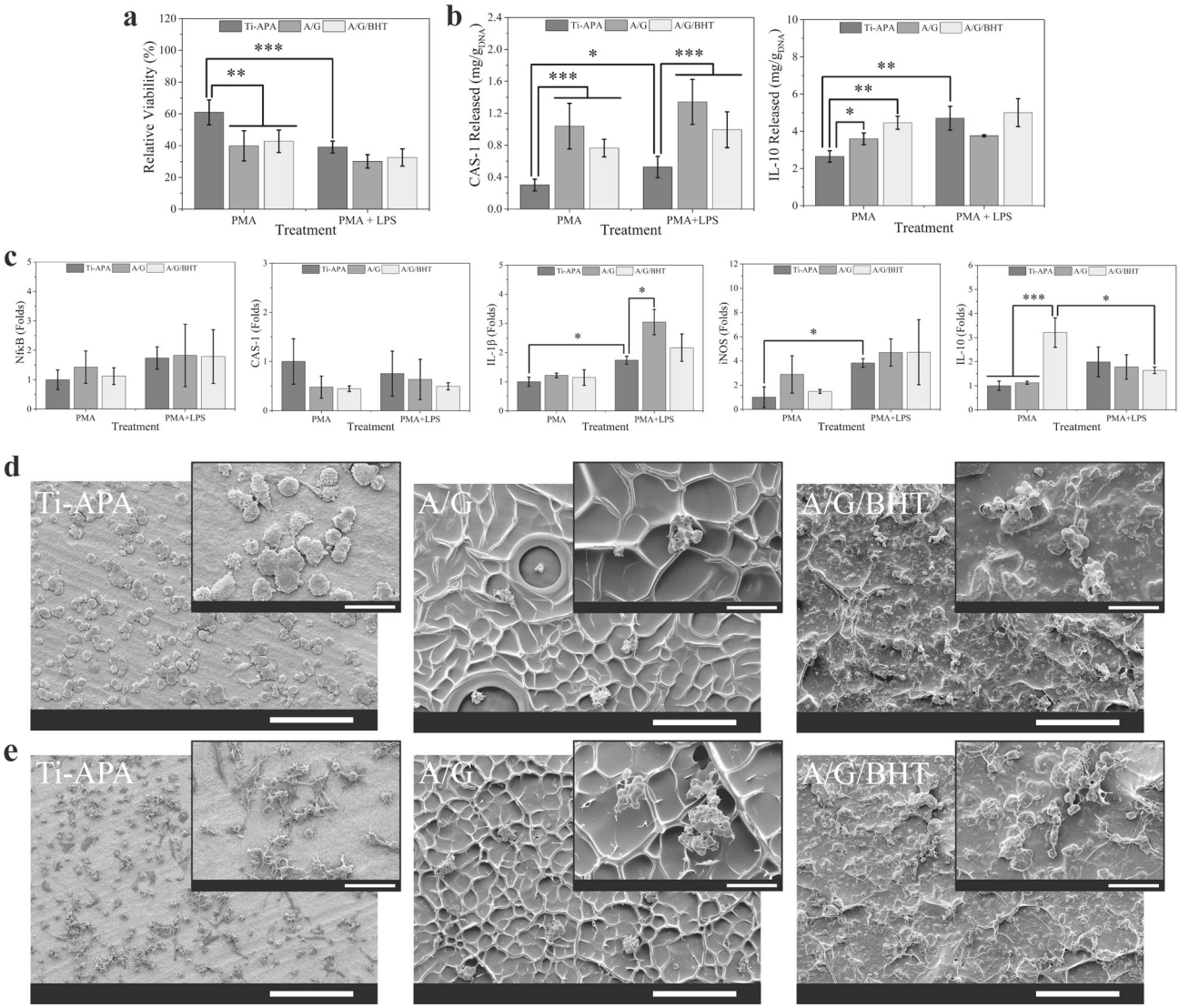

Fig. 7 Relative viability of THP-1s on various surfaces before and after treatment with LPS (**a**), CAS-1 and IL-10 release (**b**), and the expression of different genes taking part in immunological response (**c**). A/G/BHT was shown to maintain macrophage viability and was determined to be capable of exhibiting a strong acute innate response that would be resolved over time toward a pro-healing phenotype. SEM ımages of THP-1s on the surfaces before (**d**) and after (**e**) LPS treatment. THP-1s on the coating conformed into clusters and were observed not to morphologically develop into aggressive macrophages (M1), unlike Ti-APA. The ruffled morphology of M1s on Ti-APA shows that the uncoated surface could induce a chronic immunological response. The scale bars of SEM images are 200 μm and the insets are 50 μm. Statistical differences were given as *p<0.05, **p<0.01 and ***p<0.001

prevented THP-1 adhesion, unlike Ti-APA. When an important pyroptotic protein release, CAS-1 [86] was analyzed, it was observed that A/G and A/G/BHT triggered higher CAS-1 production but A/G/BHT prompted significantly higher release compared to Ti-APA (p<0.001). However, after being primed with LPS to induce extensive inflammatory reaction leading to pyroptosis, all samples demonstrated a significant increase in CAS-1 production (Fig. 7b). Ti-APA yielded a significant increase in CAS-1 production; however, A/G and A/GBHT triggered a modest increase. Nevertheless, CAS-1 produced by THP-1s on Ti-APA was still significantly lower than that on A/G and A/G/BHT (p<0.001). On the other hand, A/G/BHT prompted a significantly higher release of IL-10, a pro-healing cytokine [87], compared to Ti-APA (p<0.01) and A/G (p<0.05, Fig. 7b). After being primed with LPS, the content of IL-10 in the extracellular environment did not change for A/G and A/G/BHT, whereas a drastic increase was observed for Ti-APA (p<0.05).

NfκB is a modulator protein for inflammatory response, which takes part in osteoblast and osteoclast activities [88]. The influx of Ca^{2+}, uptake of pathogen-associated molecular patterns (PAMPs), such as LPS, could induce the signaling

cascade through the pattern recognition receptors of NfκB [89]. This further causes NfκB upregulation and the direct activation of CAS-1 and IL-1β secretion to mount pyroptotic activity. Upon the analysis of NfκB expression, both coatings induced higher expression but without statistical difference (Fig. 7c). They also demonstrated a comparable increase after LPS treatment. When further analyzing these genes, both playing role in pyroptosis, Ti-APA showed higher CAS-1 expression without a statistical difference compared to the other samples. On the other hand, it led to a lower rate of expression of IL-1β than A/G ($p<0.01$), while a similar rate was achieved with A/G/BHT. In the case of IL-10 and iNOS expression analyzed after being primed with LPS, A/G/BHT demonstrated a tremendously high IL-10 expression of THP-1s, while comparable iNOS expressions were obtained for all samples (Fig. 7c). Despite the lack of statistical differences, A/G led to the highest iNOS expression of THP-1s.

The SEM electrographs of THP-1 seeded samples were obtained after incubation with either only PMA or PMA + LPS containing media, to determine the change in cell morphology (Figs. 7d and 7e). THP-1s were observed to form clusters and appeared to protect their round shape on coatings. On the contrary, the Ti-APA surface was determined to be more provocative for THP-1s; that is, a more spread morphology with highly reactive appearance was detected. These cells, however, exhibited altered morphology under various conditions such as during PMA treatment alone (Fig. 7d) or after being primed with LPS (Fig. 7e). A/G/BHT was seen to induce a less spread morphology with clusters.

The protein production and gene expression analysis under inflammatory conditions allowed us to elucidate the immunomodulatory potential of A/G/BHT coatings. It could be concluded that none of the coatings supported mounting a prolonged and extensive inflammatory response at around the implants; however, they did not suppress the much needed early innate response, either. In a study by Rocha et al. [90], NLRP3 and CAS-1 knockout brought about the induction of alternative pathways that generated even larger pyroptotic response than increased CAS-1 production, which led to bone resorption in a periodontitis model. They further speculated that the NLRP3 signaling cascade, that is, the upregulation of NfκB and CAS-1, could attenuate a strong response against bacterial invasion while inducing the resolution of inflammatory response over time and allowing for bone remodeling. In a different study by Ma et al. [91], a diabetic model was used to show that the suppression of NfκB after the overproduction of reactive oxygen species (ROS) at a defect site could ameliorate chronic inflammatory response and reinforce osteogenesis. Hence, it is safe to consider that our findings are in line with other studies that aimed to achieve immunomodulatory response at around the implant area.

In vivo performance of coatings in a rabbit osteochondral defect model

It is discussed in the literature that inflammatory response is required for tissue regeneration and mounting a pro-healing response. Zhao et al. [92] produced a 3D scaffold structure through decellularized periosteum and reported that this natural scaffold induced a rapid increase in innate immune response, but it provided a timely resolution into the pro-healing phase. In addition, Tan et al. [93] coated an alkali-heat-treated Ti implant surface with *Lactobacillus casei* and UV-irradiated it to establish an inactivated biofilm layer. They aimed to induce rapid macrophage colonization and the prevention of film formation while deterring methicillin-resistant *Staphylococcus aureus* adhesion (MRSA), and then the release of potent osteogenic cytokines from macrophages to drive osseointegration. In addition to these findings, osteoimmunomodulatory surfaces in the literature were shown to provide results similar to our A/G/BHT in vitro data. It was demonstrated that these surfaces favored the upregulation of osteogenic/angiogenic markers such as BMP-2, ALP and VEGF-A [94]. It was also observed that an angiogenic response could be generated, as iNOS and IL-1β were downregulated while IL-10 and VEGF-A gene expressions were upregulated; however, both pro- and anti-inflammatory genes as well as the expression of inflammatory genes were shown to be maintained [95–97].

In this context, we concluded that a smooth resolution of innate immune response and a high regenerative overall response achieved with A/G/BHT in vitro would be extremely advantageous in vivo. As observed in Fig. 8b, A/G/BHT samples adhered to the surrounding bone (host bone: HB, implant: Ti) and allowed ingrowth at the end of the 1st month. New bone formation (NBF) at around the coated zone (COAT) was found (Fig. 8b). Similarly, the A/G zone showed new bone formation, but it occurred in a limited area. A/G was also observed to maintain a thick fibrous tissue, whereas a thinner and discontinuous FD was detected around A/G/BHT. All samples showed an intact marrow (BM). Overall, Ti-APA showed less new bone formation, despite that it sustained HB. Moreover, a thin but dense FD, similar to that of A/G, was detected around Ti-APA (Fig. 8b, insets).

Two months post-implantation, a strong and complete integration at around A/G/BHT samples was observed (Fig. 8b). Along with intense new bone (NB) staining, new BM (NBM) formation at the intact zones was determined. In the close-up images, NBM and NB formations coincided at the implant periphery and no damage or bone erosion occurred (Fig. 8b, insets). On the other hand, A/G coatings still maintained a thin FD around implants. Even though prematurely, these coatings demonstrated NB formation around the implants. However, there was no mature NB observed,

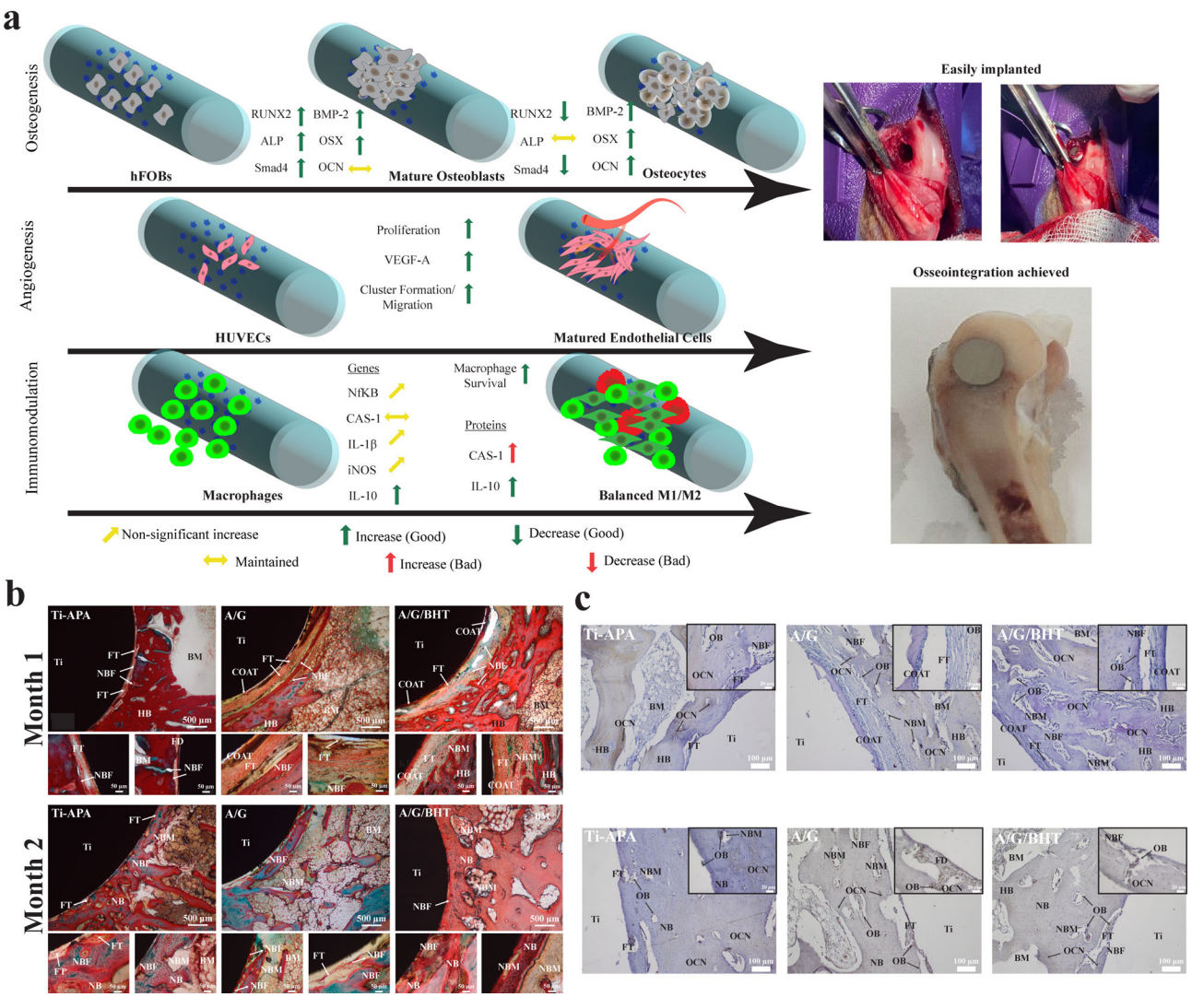

Fig. 8 Outcomes of in vitro cell culture studies (**a**), phase contrast microscope images of implant-bone slides after Masson trichrome staining (**b**), and fluorescent microscopy images of slides after IHC staining (**c**). The abbreviations used in **b** and **c** are as follows: Ti, implant; FT, fibrotic tissue; COAT, coating; NB, new bone; NBF, new bone formation; HB, host bone; BM, bone marrow; NBM, new bone marrow formation; OB, osteoblast; OCN, osteocalcin

but mature NB and a persistent HB were detected with Ti-APA-implanted samples. Unlike A/G/BHT, Ti-APA did not bring about a stable integration [98]. Having a fibrous tissue formation between implant and bone, Ti-APA and A/G were found to fail in establishing a functional bridge with host tissue (Fig. 8b).

In parallel, immunohistochemical analysis (IHC) for the OCN late osteogenic marker was conducted (Fig. 8c). The stained areas revealed that A/G/BHT samples indeed improved the rate of osseointegration [85]. Osteoblasts (OBs) colonized around the fibrotic tissue (FT) and characteristic lacuna formation were observed [99]. The intensity of OCN increased for all samples, while A/G/BHT demonstrated the highest OCN-positive staining and the presence of OBs. None of the samples showed tissue damage or chronic wound formation. In addition, a small portion of FT presence was observed in A/G/BHT, but it was diminishing in size and fully colonized by OBs. On the other hand, Ti-APA and A/G exhibited more intense FT staining (Fig. 8c). To sum up, A/G/BHT showed strong OCN staining and bone growth as well as the establishment of osteocytes around the implant area. Thus, we considered that A/G/BHT possesses immense potential to be translated into clinical use.

The highly organized immunological response toward coated implants, in addition to favorable regenerative induction with the occurrence of well-timed downstream processes, might be utilized to facilitate the vigorous integration of implant to host bone (Fig. 8a). Moreover, as reported by

Steen et al. [100], a healthy response to implants may help replace FT with NB and NBM, so that metallic implant would not be isolated due to extensive fibrosis. Although various studies focused on encouraging regeneration, they neglected the coating stability, and the physical and chemical properties. Li et al. [101] studied plasma-sprayed calcium silicate coatings, and observed good immunomodulatory, osteogenic and angiogenic response and rapid osseointegration. However, nonhomogeneous particle coating with highly dense ceramic zone facing the host bone could cause mechanical mismatch and thus micromovement in the long term. Additionally, rapid ion release might create a highly cytotoxic and inflammatory zone around the implant, leading to the aseptic erosion of bone. Direct ion implantation [102] or coating with bioactive peptides/drugs/biological factors [103] could also lead to a retention and stability problem. Therefore, having a readily swollen layer upon blood contact with the reservoir properties may help overcome most of the storage problems and allow for tailorable release ability.

In this study, we also observed that the robust and cohesive A/G/BHT did not fail during swelling or implantation in the osteochondral defect model (Fig. 8a). As one of the most often employed coating methods, the layer-by-layer approach involves mainly ionic/secondary bonding interactions. Meanwhile, the mechanical stability and shelf-life of coatings are mostly overlooked, which are due to the weak cohesion of coated layer or rapid degradation due to insufficient crosslinking [104, 105]. Here, we coated the surface of implants with an alginate layer to both facilitate the homogeneous diffusion of A/G/BHT layer and amplify surface-polymer network bond availability and intramolecular crosslinking without agglomeration.

Owing to the aforementioned structural and physical properties, as well as ECM-like chemistry, the composite A/G/BHT layer demonstrated good potential as a multifunctional coating. These samples scored the highest in terms of various aspects of osseointegration by the end of the 2-month evaluation period (Table 5). The overall scores demonstrated that A/G coatings were not as successful as either Ti-APA or A/G/BHT. In addition, Ti-APA without a coating did not show satisfactory performance, since FD was maintained and failed to induce NB formation to the extent that A/G/BHT did.

Fisher et al. [106] argued that future implant surfaces would be immune-instructive to govern all biological responses, to achieve robust osseointegration. It was pointed out that these surfaces could be a combination of ECM-like composite hydrogel coatings and multifunctional peptides/cells/exosomes, for the ability to increase control over the biological mechanisms at play. To this end, Rondanelli et al. [107] reviewed various studies analyzing the effect of B containing molecules and indicated that B is actually a modulator of Ca metabolism, hence could act as a switch for various metabolic activities.

Table 5 Osseointegration scores of samples at the 1st and 2nd month post-implantation (n=4)

Sample	Score	
	Month 1	Month 2
Ti-APA	4.25±1.50	4.00±1.15[a]
A/G	2.25±0.95	2.75±0.50
A/G/BHT	2.50±0.58	4.50±0.58[b]

The scoring was performed in accordance with Masson trichrome staining results

[a]Ti-APA demonstrated a deterioration where only the APA modification appeared to be insufficient for establishing a functional bridge between the host bone and Ti

[b]A/G/BHT could immensely reinforce the osseointegration capacity of the Ti implant. It showed a significant increase in score from the 1st to the 2nd month after implant placement

Conclusions

As a promising interphase structure, the structural, morphological, mechanical, and chemical properties of A/G-based coatings were presented and discussed in our previous study. Herein, we doped HT with B and loaded it in A/G to improve the biological properties of implants. A/G/BHT was designed to mimic the ECM ultrastructure due to its similarities with bone ECM, good stiffness, microscopic roughness, and the release of bioactive ions. Hence, its intrinsic hydrogel-related properties, such as good cohesion, high water uptake, extremely low pre-gel viscosity and tailorable degradation rate to coincide with the development of new bone, might have endowed it with unmatched regenerative and immunomodulatory properties. The A/G/BHT samples exhibited high mechanical strength, cohesiveness and surface roughness. At the same time, they demonstrated high capacity to support osteoblast and endothelial cell adhesion and growth. Our experimental results suggest that A/G/BHT can be used as a reservoir for custom-made peptides, antibacterial agents, regenerative factors or disease-specific drugs such as anti-osteoporotic agents, such that these may be released with greater control in terms of rate and concentration, and directly target the defect zone. The proposed A/G/BHT layer on Ti demonstrated immense potential in provoking an early innate immune response, which could rapidly be resolved into a pro-healing/regenerative phenotype, in addition to beneficial osteogenic and angiogenic properties. Therefore, it could be stated that the versatility of the proposed gap-filling composite coating had been proven, and it can be employed in

regular/irregularly shaped implants in bone tissue engineering.

Supplementary Information The online version contains supplementary material available at https://doi.org/10.1007/s42242-022-00218-y.

Acknowledgements Authors would like to thank Center of Excellence in Biomaterials and Tissue Engineering (BIOMATEN) for the support provided. Authors also acknowledge financial support provided by National Boron Institute (BOREN, Grant No: 2018-31-07-25-001).

Author contributions Conceptualization: AEP, KA, ZE and AT; methodology: AEP, TD and MVY; data analysis: AEP and TD; writing—original draft preparation: AEP; writing—review and editing: DK, ZE and AT; ZE provided sources; KA, ZE and AT performed supervision. All authors have read and agreed to the published version of the manuscript.

Declarations

Conflict of interest The authors declare that they have no conflict of interest.

Ethical approval All animal procedures in our study were approved by the Institutional Animal Care and Use Committee of Afyon Kocatepe University (Date: 18.09.2018, Decision No.: 49533702/147).

Data availability The data that support the findings of this study are available from the corresponding author upon reasonable request.

References

1. Rony L, Aguado E, Verlee B et al (2021) Microarchitecture of titanium cylinders obtained by additive manufacturing does not influence osseointegration in the sheep. Regen Biomater 8(4):rbab021. https://doi.org/10.1093/rb/rbab021
2. Prestat M, Thierry D (2021) Corrosion of titanium under simulated inflammation conditions: clinical context and in vitro investigations. Acta Biomater 136:72–87. https://doi.org/10.1016/j.actbio.2021.10.002
3. Lee H, Lee MK, Han G et al (2022) Customizable design of multiple-biomolecule delivery platform for enhanced osteogenic responses via 'tailored assembly system.' Bio-Des Manuf 5(3):451–464. https://doi.org/10.1007/s42242-022-00190-7
4. Koons GL, Diba M, Mikos AG (2020) Materials design for bone-tissue engineering. Nat Rev Mater 5(8):584–603. https://doi.org/10.1038/s41578-020-0204-2
5. Zhang XX, Lv Y, Lei Y et al (2021) Enhancement of corrosion resistance and biological performances of Cu-incorporated hydroxyapatite/TiO_2 coating by adjusting Cu chemical configuration and hydroxyapatite contents. ACS Appl Bio Mater 4(1):903–917. https://doi.org/10.1021/acsabm.0c01390
6. Švagrová K, Horkavcová D, Jablonská E et al (2022) Titania-based sol-gel coatings with Ag, Ca-P applied on titanium substrate developed for implantation. J Biomed Mater Res B Appl Biomater 110(1):115–124. https://doi.org/10.1002/jbm.b.34895
7. Querido W, Rossi AL, Farina M (2016) The effects of strontium on bone mineral: a review on current knowledge and microanalytical approaches. Micron 80:122–134. https://doi.org/10.1016/j.micron.2015.10.006
8. Davis R, Singh A, Jackson MJ et al (2022) A comprehensive review on metallic implant biomaterials and their subtractive manufacturing. Int J Adv Manuf Technol 120(3–4):1473–1530. https://doi.org/10.1007/s00170-022-08770-8
9. Guo CY, Matinlinna JP, Tang AT (2012) Effects of surface charges on dental implants: past, present, and future. Int J Biomater 2012:381535. https://doi.org/10.1155/2012/381535
10. Silva-Bermudez P, Rodil S (2013) An overview of protein adsorption on metal oxide coatings for biomedical implants. Surf Coat Technol 233:147–158. https://doi.org/10.1016/j.surfcoat.2013.04.028
11. Pazarçeviren AE, Tezcaner A, Evis Z (2021) Multifunctional natural polymer-based metallic implant surface modifications. Biointerphases 16(2):020803. https://doi.org/10.1116/6.0000876
12. Kuo YJ, Chen CH, Dash P et al (2022) Angiogenesis, osseointegration, and antibacterial applications of polyelectrolyte multilayer coatings incorporated with silver/strontium containing mesoporous bioactive glass on 316L stainless steel. Front Bioeng Biotechnol 10:818137. https://doi.org/10.3389/fbioe.2022.818137
13. Jariya SAI, Babu AA, Narayanan TSN et al (2022) Development of a novel smart carrier for drug delivery: ciprofloxacin loaded vaterite/reduced graphene oxide/PCL composite coating on TiO_2 nanotube coated titanium. Ceramics Int 48(7):9579–9594. https://doi.org/10.1016/j.ceramint.2021.12.156
14. Moskalewicz T, Warcaba M, Łukaszczyk A et al (2022) Electrophoretic deposition, microstructure and properties of multi-component sodium alginate-based coatings incorporated with graphite oxide and hydroxyapatite on titanium biomaterial substrates. Appl Surf Sci 575:151688. https://doi.org/10.1016/j.apsusc.2021.151688
15. Jing W, Feng L, Wang B et al (2021) Polymer-ceramic fiber nanocomposite coatings on titanium metal implant devices for diseased bone tissue regeneration. J Sci Adv Mater Dev 6(3):399–406. https://doi.org/10.1016/j.jsamd.2021.04.001
16. Mariani E, Lisignoli G, Borzì RM et al (2019) Biomaterials: foreign bodies or tuners for the immune response? Int J Mol Sci 20(3):636. https://doi.org/10.3390/ijms20030636
17. Szekalska M, Puciłowska A, Szymańska E et al (2016) Alginate: current use and future perspectives in pharmaceutical and biomedical applications. Int J Polym Sci 2016:17. https://doi.org/10.1155/2016/7697031
18. Tsou YH, Khoneisser J, Huang PC et al (2016) Hydrogel as a bioactive material to regulate stem cell fate. Bioact Mater 1(1):39–55. https://doi.org/10.1016/j.bioactmat.2016.05.001
19. Wang D, Zhu Y, Huang Y et al (2021) Pancreatic extracellular matrix/alginate hydrogels provide a supportive microenvironment for insulin-producing cells. ACS Biomater Sci Eng 7(8):3793–3805. https://doi.org/10.1021/acsbiomaterials.1c00269
20. Chan AW, Neufeld RJ (2009) Modeling the controllable pH-responsive swelling and pore size of networked alginate based biomaterials. Biomaterials 30(30):6119–6129. https://doi.org/10.1016/j.biomaterials.2009.07.034
21. Andersen T, Auk-Emblem P, Dornish M (2015) 3D cell culture in alginate hydrogels. Microarrays 4(2):133–161. https://doi.org/10.3390/microarrays4020133
22. Zhang X, Morits M, Jonkergouw C et al (2020) Three-dimensional printed cell culture model based on spherical colloidal lignin particles and cellulose nanofibril-alginate hydrogel. Biomacromolecules 21(5):1875–1885. https://doi.org/10.1021/acs.biomac.9b01745
23. Cavo M, Caria M, Pulsoni I et al (2018) A new cell-laden 3D Alginate-Matrigel hydrogel resembles human breast cancer cell malignant morphology, spread and invasion capability observed "in vivo." Sci Rep 8(1):5333. https://doi.org/10.1038/s41598-018-23250-4

24. Wang B, Díaz-Payno PJ, Browe DC et al (2021) Affinity-bound growth factor within sulfated interpenetrating network bioinks for bioprinting cartilaginous tissues. Acta Biomater 128:130–142. https://doi.org/10.1016/j.actbio.2021.04.016
25. Oh GW, Kim SC, Kim TH et al (2021) Characterization of an oxidized alginate-gelatin hydrogel incorporating a COS-salicylic acid conjugate for wound healing. Carbohydr Polym 252:117145. https://doi.org/10.1016/j.carbpol.2020.117145
26. Dodero A, Alberti S, Gaggero G et al (2021) An up-to-date review on alginate nanoparticles and nanofibers for biomedical and pharmaceutical applications. Adv Mater Interf 8(22):2100809. https://doi.org/10.1002/admi.202100809
27. Sarker B, Rompf J, Silva R et al (2015) Alginate-based hydrogels with improved adhesive properties for cell encapsulation. Int J Biol Macromol 78:72–78. https://doi.org/10.1016/j.ijbiomac.2015.03.061
28. Hasturk O, Jordan KE, Choi J et al (2020) Enzymatically crosslinked silk and silk-gelatin hydrogels with tunable gelation kinetics, mechanical properties and bioactivity for cell culture and encapsulation. Biomaterials 232:119720. https://doi.org/10.1016/j.biomaterials.2019.119720
29. Heltmann-Meyer S, Steiner D, Müller C et al (2021) Gelatin methacryloyl is a slow degrading material allowing vascularization and long-term use in vivo. Biomed Mater 16(6):065004. https://doi.org/10.1088/1748-605X/ac1e9d
30. Wang X, Ao Q, Tian X et al (2017) Gelatin-based hydrogels for organ 3D bioprinting. Polymers 9(9):401. https://doi.org/10.3390/polym9090401
31. Erkoc P, Uvak I, Nazeer MA et al (2020) 3D printing of cytocompatible gelatin-cellulose-alginate blend hydrogels. Macromol Biosci 20(10):e2000106. https://doi.org/10.1002/mabi.202000106
32. Ghanbari M, Salavati-Niasari M, Mohandes F (2021) Injectable hydrogels based on oxidized alginate-gelatin reinforced by carbon nitride quantum dots for tissue engineering. Int J Pharm 602:120660. https://doi.org/10.1016/j.ijpharm.2021.120660
33. Flores-Torres S, Peza-Chavez O, Kuasne H et al (2021) Alginate-gelatin-Matrigel hydrogels enable the development and multigenerational passaging of patient-derived 3D bioprinted cancer spheroid models. Biofabrication 13(2):025001. https://doi.org/10.1088/1758-5090/abdb87
34. Sun CK, Ke CJ, Lin YW et al (2021) Transglutaminase cross-linked gelatin-alginate-antibacterial hydrogel as the drug delivery-coatings for implant-related infections. Polymers 13(3):414. https://doi.org/10.3390/polym13030414
35. Chalitangkoon J, Wongkittisin M, Monvisade P (2020) Silver loaded hydroxyethylacryl chitosan/sodium alginate hydrogel films for controlled drug release wound dressings. Int J Biol Macromol 159:194–203. https://doi.org/10.1016/j.ijbiomac.2020.05.061
36. Xue W, Liu B, Zhang H et al (2022) Controllable fabrication of alginate/poly-L-ornithine polyelectrolyte complex hydrogel networks as therapeutic drug and cell carriers. Acta Biomater 138:182–192. https://doi.org/10.1016/j.actbio.2021.11.004
37. Liu Y, Hu Q, Dong W et al (2022) Alginate/gelatin-based hydrogel with soy protein/peptide powder for 3D printing tissue-engineering scaffolds to promote angiogenesis. Macromol Biosci 22(4):e2100413. https://doi.org/10.1002/mabi.202100413
38. Pazarçeviren AE, Akbaba S, Tezcaner A et al (2022) Seamless and robust alginate/gelatin coating on Ti-6Al-4V as a gap filling interphase. Appl Surf Sci 581:152393. https://doi.org/10.1016/j.apsusc.2021.152393
39. Pazarçeviren AE, Tezcaner A, Keskin D et al (2021) Boron-doped biphasic hydroxyapatite/β-tricalcium phosphate for bone tissue engineering. Biol Trace Elem Res 199(3):968–980. https://doi.org/10.1007/s12011-020-02230-8
40. Çiftci Dede E, Korkusuz P, Bilgiç E et al (2022) Boron nano-hydroxyapatite composite increases the bone regeneration of ovariectomized rabbit femurs. Biol Trace Elem Res 200(1):183–196. https://doi.org/10.1007/s12011-021-02626-0
41. Chen S, Michálek M, Galusková D et al (2020) Multi-targeted B and Co co-doped 45S5 bioactive glasses with angiogenic potential for bone regeneration. Mater Sci Eng C Mater Biol Appl 112:110909. https://doi.org/10.1016/j.msec.2020.110909
42. Fu SY, Feng XQ, Lauke B et al (2008) Effects of particle size, particle/matrix interface adhesion and particle loading on mechanical properties of particulate–polymer composites. Composites Part B Eng 39(6):933–961. https://doi.org/10.1016/j.compositesb.2008.01.002
43. Maji K, Dasgupta S, Bhaskar R et al (2020) Photo-crosslinked alginate nano-hydroxyapatite paste for bone tissue engineering. Biomed Mater 15(5):055019. https://doi.org/10.1088/1748-605X/ab9551
44. Carpentier G, Berndt S, Ferratge S et al (2020) Angiogenesis analyzer for ImageJ—a comparative morphometric analysis of "Endothelial Tube Formation Assay" and "Fibrin Bead Assay." Sci Rep 10(1):11568. https://doi.org/10.1038/s41598-020-67289-8
45. Otsuki B, Takemoto M, Fujibayashi S et al (2006) Pore throat size and connectivity determine bone and tissue ingrowth into porous implants: three-dimensional micro-CT based structural analyses of porous bioactive titanium implants. Biomaterials 27(35):5892–5900. https://doi.org/10.1016/j.biomaterials.2006.08.013
46. Brokesh AM, Gaharwar AK (2020) Inorganic biomaterials for regenerative medicine. ACS Appl Mater Interf 12(5):5319–5344. https://doi.org/10.1021/acsami.9b17801
47. Gizer M, Köse S, Karaosmanoglu B et al (2020) The effect of boron-containing nano-hydroxyapatite on bone cells. Biol Trace Elem Res 193(2):364–376. https://doi.org/10.1007/s12011-019-01710-w
48. Balasubramanian P, Hupa L, Jokic B et al (2017) Angiogenic potential of boron-containing bioactive glasses: in vitro study. J Mater Sci 52:8785–8792. https://doi.org/10.1007/s10853-016-0563-7
49. Li K, Lu X, Razanau I et al (2019) The enhanced angiogenic responses to ionic dissolution products from a boron-incorporated calcium silicate coating. Mater Sci Eng C Mater Biol Appl 101:513–520. https://doi.org/10.1016/j.msec.2019.04.009
50. Baniwal SK, Shah PK, Shi Y et al (2012) Runx2 promotes both osteoblastogenesis and novel osteoclastogenic signals in ST2 mesenchymal progenitor cells. Osteoporos Int 23(4):1399–1413. https://doi.org/10.1007/s00198-011-1728-5
51. Yahiro Y, Maeda S, Morikawa M et al (2020) BMP-induced Atoh8 attenuates osteoclastogenesis by suppressing Runx2 transcriptional activity and reducing the Rankl/Opg expression ratio in osteoblasts. Bone Res 8(1):32. https://doi.org/10.1038/s41413-020-00106-0
52. Chen D, Gong Y, Xu L et al (2019) Bidirectional regulation of osteogenic differentiation by the FOXO subfamily of Forkhead transcription factors in mammalian MSCs. Cell Prolif 52(2):e12540. https://doi.org/10.1111/cpr.12540
53. Duman E, Şahin Kehribar E, Ahan RE et al (2019) Biomineralization of calcium phosphate crystals controlled by protein-protein interactions. ACS Biomater Sci Eng 5(9):4750–4763. https://doi.org/10.1021/acsbiomaterials.9b00649
54. Shekaran A, Shoemaker JT, Kavanaugh TE et al (2014) The effect of conditional inactivation of beta 1 integrins using twist 2 Cre, Osterix Cre and osteocalcin Cre lines on skeletal phenotype. Bone 68:131–141. https://doi.org/10.1016/j.bone.2014.08.008
55. Kargozar S, Baino F, Hamzehlou S et al (2018) Bioactive glasses: sprouting angiogenesis in tissue engineering. Trends biotechnol 36(4):430–444. https://doi.org/10.1016/j.tibtech.2017.12.003

56. Westhauser F, Widholz B, Nawaz Q et al (2019) Favorable angiogenic properties of the borosilicate bioactive glass 0106-B1 result in enhanced in vivo osteoid formation compared to 45S5 Bioglass. Biomater Sci 7(12):5161–5176. https://doi.org/10.1039/c9bm01220f
57. Şen Ö, Emanet M, Çulha M (2019) Stimulatory effect of hexagonal boron nitrides in wound healing. ACS Appl Bio Mater 2(12):5582–5596. https://doi.org/10.1021/acsabm.9b00669
58. Raines AL, Berger MB, Patel N et al (2019) VEGF-A regulates angiogenesis during osseointegration of Ti implants via paracrine/autocrine regulation of osteoblast response to hierarchical microstructure of the surface. J Biomed Mater Res A 107(2):423–433. https://doi.org/10.1002/jbm.a.36559
59. Hu K, Olsen BR (2016) The roles of vascular endothelial growth factor in bone repair and regeneration. Bone 91:30–38. https://doi.org/10.1016/j.bone.2016.06.013
60. Yu P, Zhang X, Liu N et al (2021) Pyroptosis: mechanisms and diseases. Signal Transduct Target Ther 6(1):128. https://doi.org/10.1038/s41392-021-00507-5
61. Zhang R, Liu X, Xiong Z et al (2018) The immunomodulatory effects of Zn-incorporated micro/nanostructured coating in inducing osteogenesis. Artif Cells Nanomed Biotechnol 46(sup1):1123–1130. https://doi.org/10.1080/21691401.2018.1446442
62. Dollinger C, Ndreu-Halili A, Uka A et al (2017) Controlling incoming macrophages to implants: responsiveness of macrophages to gelatin micropatterns under M1/M2 phenotype defining biochemical stimulations. Adv Biosyst 1(6):1700041. https://doi.org/10.1002/adbi.201700041
63. Floquet CF, Sieben VJ, MacKay BA et al (2016) Determination of boron in produced water using the carminic acid assay. Talanta 150:240–252. https://doi.org/10.1016/j.talanta.2015.12.010
64. Su Y, Huang C, Lu F et al (2018) Alginate affects agglomeration state and uptake of 14C-labeled few-layer graphene by freshwater snails: implications for the environmental fate of graphene in aquatic systems. Environ Pollut 234:513–522. https://doi.org/10.1016/j.envpol.2017.11.087
65. Narayanan A, Kaur S, Peng C et al (2019) Viscosity attunes the adhesion of bioinspired low modulus polyester adhesive sealants to wet tissues. Biomacromolecules 20(7):2577–2586. https://doi.org/10.1021/acs.biomac.9b00383
66. Tiu BDB, Delparastan P, Ney MR et al (2019) Enhanced adhesion and cohesion of bioinspired dry/wet pressure-sensitive adhesives. ACS Appl Mater Interf 11(31):28296–28306. https://doi.org/10.1021/acsami.9b08429
67. Ratanavaraporn J, Chuma N, Kanokpanont S et al (2019) Beads fabricated from alginate, hyaluronic acid, and gelatin using ionic crosslinking and layer-by-layer coating techniques for controlled release of gentamicin. J Appl Polym Sci 136(1):46893. https://doi.org/10.1002/app.46893
68. Jing X, Sun Y, Liu Y et al (2021) Alginate/chitosan-based hydrogel loaded with gene vectors to deliver polydeoxyribonucleotide for effective wound healing. Biomater Sci 9(16):5533–5541. https://doi.org/10.1039/d1bm00911g
69. Reddy MSB, Ponnamma D, Choudhary R et al (2021) A comparative review of natural and synthetic biopolymer composite scaffolds. Polymers 13(7):1105. https://doi.org/10.3390/polym13071105
70. Zhang X, Wang K, Hu JY et al (2020) Role of a high calcium ion content in extending the properties of alginate dual-crosslinked hydrogels. J Mater Chem A 8(47):25390–25401. https://doi.org/10.1039/D0TA09315G
71. Davidenko N, Schuster CF, Bax DV et al (2016) Evaluation of cell binding to collagen and gelatin: a study of the effect of 2D and 3D architecture and surface chemistry. J Mater Sci Mater Med 27(10):148. https://doi.org/10.1007/s10856-016-5763-9
72. Stubbe B, Mignon A, Declercq H et al (2019) Development of gelatin-alginate hydrogels for burn wound treatment. Macromol Biosci 19(8):e1900123. https://doi.org/10.1002/mabi.201900123
73. Hosseini S, Naderi-Manesh H, Vali H et al (2019) Contribution of osteocalcin-mimetic peptide enhances osteogenic activity and extracellular matrix mineralization of human osteoblast-like cells. Colloids Surf B Biointerf 173:662–671. https://doi.org/10.1016/j.colsurfb.2018.10.035
74. Moon YJ, Yun CY, Choi H et al (2016) Smad4 controls bone homeostasis through regulation of osteoblast/osteocyte viability. Exp Mol Med 48(9):e256. https://doi.org/10.1038/emm.2016.75
75. Tenkumo T, Vanegas Sáenz JR, Nakamura K et al (2018) Prolonged release of bone morphogenetic protein-2 in vivo by gene transfection with DNA-functionalized calcium phosphate nanoparticle-loaded collagen scaffolds. Mater Sci Eng C Mater Biol Appl 92:172–183. https://doi.org/10.1016/j.msec.2018.06.047
76. Yan J, Li J, Hu J et al (2018) Smad4 deficiency impairs chondrocyte hypertrophy via the Runx2 transcription factor in mouse skeletal development. J Biol Chem 293(24):9162–9175. https://doi.org/10.1074/jbc.RA118.001825
77. Liu YS, Liu YA, Huang CJ et al (2015) Mechanosensitive TRPM7 mediates shear stress and modulates osteogenic differentiation of mesenchymal stromal cells through Osterix pathway. Sci Rep 5:16522. https://doi.org/10.1038/srep16522
78. Moon YJ, Yun CY, Choi H et al (2018) Osterix regulates cortical-ization for longitudinal bone growth via integrin β3 expression. Exp Mol Med 50(7):1–11. https://doi.org/10.1038/s12276-018-0119-9
79. Stich T, Alagboso F, Křenek T et al (2021) Implant-bone-interface: reviewing the impact of titanium surface modifications on osteogenic processes in vitro and in vivo. Bioeng Transl Med 7(1):e10239. https://doi.org/10.1002/btm2.10239
80. Su T, Zheng A, Cao L et al (2022) Adhesion-enhancing coating embedded with osteogenesis-promoting PDA/HA nanoparticles for peri-implant soft tissue sealing and osseointegration. Bio-Des Manuf 5(2):233–248. https://doi.org/10.1007/s42242-022-00184-5
81. Farzin A, Hassan S, Teixeira LSM et al (2021) Self-oxygenation of tissues orchestrates full-thickness vascularization of living implants. Adv Funct Mater 31(42):2100850. https://doi.org/10.1002/adfm.202100850
82. Kocherova I, Bryja A, Mozdziak P et al (2019) Human umbilical vein endothelial cells (HUVECs) co-culture with osteogenic cells: from molecular communication to engineering prevascularised bone grafts. J Clin Med 8(10):1602. https://doi.org/10.3390/jcm8101602
83. Dashnyam K, Buitrago JO, Bold T et al (2019) Angiogenesis-promoted bone repair with silicate-shelled hydrogel fiber scaffolds. Biomater Sci 7(12):5221–5231. https://doi.org/10.1039/c9bm01103j
84. Trujillo S, Gonzalez-Garcia C, Rico P et al (2020) Engineered 3D hydrogels with full-length fibronectin that sequester and present growth factors. Biomaterials 252:120104. https://doi.org/10.1016/j.biomaterials
85. Li J, Liu X, Crook JM et al (2020) 3D printing of cytocompatible graphene/alginate scaffolds for mimetic tissue constructs. Front Bioeng Biotechnol 8:824. https://doi.org/10.3389/fbioe.2020.00824
86. Vande Walle L, Lamkanfi M (2011) Inflammasomes: caspase-1-activating platforms with critical roles in host defense. Front Microbiol 2:3. https://doi.org/10.3389/fmicb.2011.00003
87. Tan F, Al-Rubeai M (2021) A multifunctional dexamethasone-delivery implant fabricated using atmospheric plasma and its effects on apoptosis, osteogenesis and inflammation. Drug Deliv

Transl Res 11(1):86–102. https://doi.org/10.1007/s13346-019-00700-8
88. Lin TH, Pajarinen J, Lu L et al (2017) NF-κB as a therapeutic target in inflammatory-associated bone diseases. Adv Protein Chem Struct Biol 107:117–154. https://doi.org/10.1016/bs.apcsb.2016.11.002
89. Yu C, Zhang C, Kuang Z et al (2021) The role of NLRP3 inflammasome activities in bone diseases and vascular calcification. Inflammation 44(2):434–449. https://doi.org/10.1007/s10753-020-01357-z
90. Rocha FRG, Delitto AE, de Souza JAC et al (2020) Relevance of Caspase-1 and NLRP3 inflammasome on inflammatory bone resorption in a murine model of periodontitis. Sci Rep 10(1):7823. https://doi.org/10.1038/s41598-020-64685-y
91. Ma XY, Cui D, Wang Z et al (2022) Silk fibroin/hydroxyapatite coating improved osseointegration of porous titanium implants under diabetic conditions via activation of the PI3K/Akt signaling pathway. ACS Biomater Sci Eng 8(7):2908–2919. https://doi.org/10.1021/acsbiomaterials.2c00023
92. Zhao C, Qiu P, Li M et al (2021) The spatial form periosteal-bone complex promotes bone regeneration by coordinating macrophage polarization and osteogenic-angiogenic events. Mater Today Bio 12:100142. https://doi.org/10.1016/j.mtbio.2021.100142
93. Tan L, Fu J, Feng F et al (2020) Engineered probiotics biofilm enhances osseointegration via immunoregulation and anti-infection. Sci Adv 6(46):eaba5723. https://doi.org/10.1126/sciadv.aba5723
94. He M, Gao X, Fan Y et al (2021) Tannic acid/Mg^{2+}-based versatile coating to manipulate the osteoimmunomodulation of implants. J Mater Chem B 9(4):1096–1106. https://doi.org/10.1039/d0tb01577f
95. Peng F, Qiu L, Yao M et al (2021) A lithium-doped surface inspires immunomodulatory functions for enhanced osteointegration through PI3K/AKT signaling axis regulation. Biomater Sci 9(24):8202–8220. https://doi.org/10.1039/d1bm01075a
96. Chen M, Hu J, Zhang E et al (2021) The osteoimmunomodulatory effect of nanostructured TiF_x/TiO_x coating on osteogenesis induction. Biomed Mater 16(4):045041. https://doi.org/10.1088/1748-605X/ac0863
97. Ding T, Kang W, Li J et al (2021) An in situ tissue engineering scaffold with growth factors combining angiogenesis and osteoimmunomodulatory functions for advanced periodontal bone regeneration. J Nanobiotechnol 19(1):247. https://doi.org/10.1186/s12951-021-00992-4
98. Ma Z, He HT, Deng CX et al (2022) 3D bioprinting of proangiogenic constructs with induced immunomodulatory microenvironments through a dual cross-linking procedure using laponite incorporated bioink. Composites Part B Eng 229:109399. https://doi.org/10.1016/j.compositesb.2021.109399
99. Shi J, Sun J, Zhang W et al (2016) Demineralized bone matrix scaffolds modified by CBD-SDF-1α promote bone regeneration via recruiting endogenous stem cells. ACS Appl Mater Interf 8(41):27511–27522. https://doi.org/10.1021/acsami.6b08685
100. Steen EH, Wang X, Balaji S et al (2020) The role of the anti-inflammatory cytokine Interleukin-10 in tissue fibrosis. Adv Wound Care 9(4):184–198. https://doi.org/10.1089/wound.2019.1032
101. Li K, Lu X, Liu S et al (2021) Boron-incorporated micro/nano-topographical calcium silicate coating dictates osteo/angiogenesis and inflammatory response toward enhanced osseointegration. Biol Trace Elem Res 199(10):3801–3816. https://doi.org/10.1007/s12011-020-02517-w
102. Wang L, Luo Q, Zhang X et al (2020) Co-implantation of magnesium and zinc ions into titanium regulates the behaviors of human gingival fibroblasts. Bioact Mater 6(1):64–74. https://doi.org/10.1016/j.bioactmat.2020.07.012
103. Palkowitz AL, Tuna T, Bishti S et al (2021) Biofunctionalization of dental abutment surfaces by crosslinked ECM proteins strongly enhances adhesion and proliferation of gingival fibroblasts. Adv Healthc Mater 10(10):e2100132. https://doi.org/10.1002/adhm.202100132
104. Chen W, Xu K, Tao B et al (2018) Multilayered coating of titanium implants promotes coupled osteogenesis and angiogenesis in vitro and in vivo. Acta Biomater 74:489–504. https://doi.org/10.1016/j.actbio.2018.04.043
105. Zheng W, Chen C, Zhang X et al (2021) Layer-by-layer coating of carboxymethyl chitosan gelatin-alginate on cotton gauze for hemostasis and wound healing. Surf Coat Technol 406:126644. https://doi.org/10.1016/j.surfcoat.2020.126644
106. Fisher LE, Kämmerling L, Alexander MR et al (2022) Immune-instructive materials as new tools for immunotherapy. Curr Opin Biotechnol 74:194–203. https://doi.org/10.1016/j.copbio.2021.11.005
107. Rondanelli M, Faliva MA, Peroni G et al (2020) Pivotal role of boron supplementation on bone health: a narrative review. J Trace Elem Med Biol 62:126577. https://doi.org/10.1016/j.jtemb.2020.126577